# Snapping Deployable Toroids for Modular Gridshells

FELIX DELLINGER, TU Wien, Austria
MARTIN KILIAN, TU Wien, Austria
MUNKYUN LEE, University of Tokyo, Japan
CHRISTIAN MÜLLER, TU Wien, Austria
GEORG NAWRATIL, TU Wien, Austria
TOMOHIRO TACHI, University of Tokyo, Japan
KIUMARS SHARIFMOGHADDAM, TU Wien, Austria

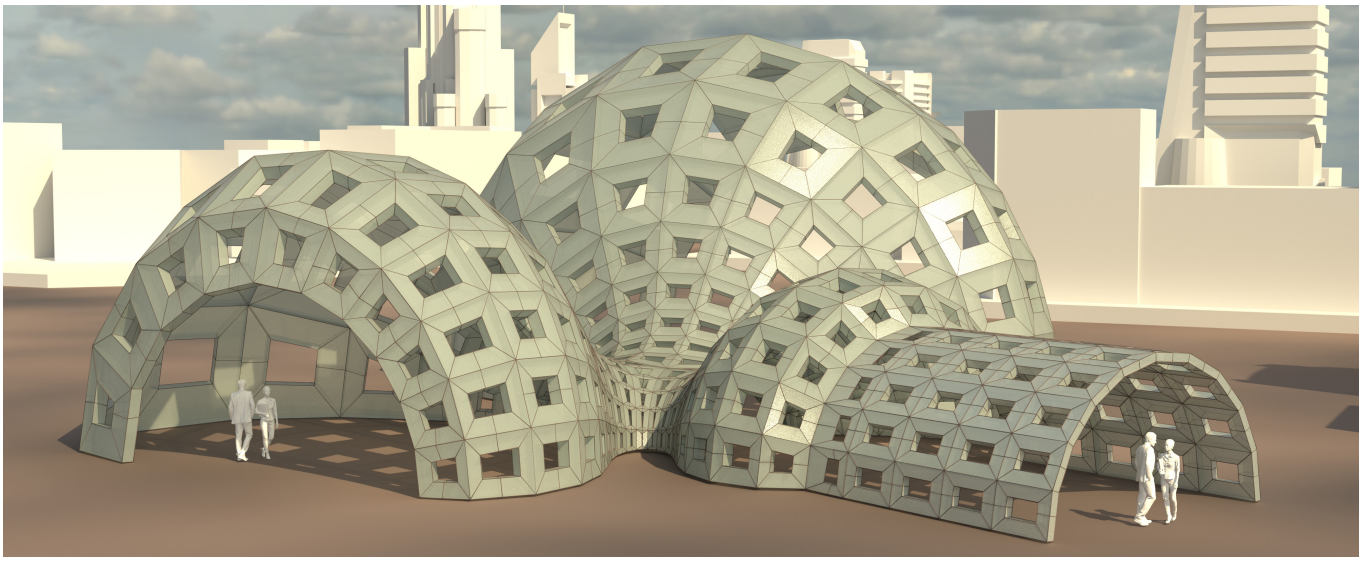

Fig. 1. Snapping deployable toroid structure. Concept of a lightweight pavilion of multistable toroidal modules. Each individual module is a polyhedral torus that admits two isometric configurations: the deployed state as depicted but also a flat-folded state (see Figs. 2 and 21). In both states corresponding faces are congruent to each other, only the angles at the edges (hinges) are different. There is no continuous motion from one state to the other but a snapping motion is possible due to the flexibility of the material.

We introduce a novel class of polyhedral tori (PQ-toroids) that snap between two stable configurations – a flat state and a deployed one separated by an energy barrier. Being able to create PQ-toroids from any set of given planar bottom and side faces opens the possibility to assemble the bistable blocks into a thick freeform curved shell structure to follow a planar quadrilateral (PQ) net with coplanar adjacent offset directions.

A design pipeline is developed and presented for inversely computing PQ-toroid modules using conjugate net decompositions of a given surface. We analyze the snapping behavior and energy barriers through simulation and build physical prototypes to validate the feasibility of the proposed system.

This work expands the geometric design space of multistable origami for lightweight modular structures and offers practical applications in architectural and deployable systems.

CCS Concepts: • **Computing methodologies → Shape modeling**.

Additional Key Words and Phrases: Multistable Origami, Deployable Structures, Flat-Foldability, Conjugate Nets, Reprogrammable Modules, Origami-Based Architecture, Computational Design, Lightweight Gridshells

Authors' Contact Information: Felix Dellinger, felix.dellinger@tuwien.ac.at, Inst. of Discr. Math. and Geometry, TU Wien, Austria; Martin Kilian, martin.kilian@tuwien.ac.at, Inst. of Discr. Math. and Geometry, TU Wien, Austria; Munkyun Lee, tokyo2021lmk@g.ecc.u-tokyo.ac.jp, Department of General Systems Studies, University of Tokyo, Japan; Christian Müller, christian.mueller@tuwien.ac.at, Inst. of Discr. Math. and Geometry, TU Wien, Austria; Georg Nawratil, georg.nawratil@tuwien.ac.at, Inst. of Discr. Math. and Geometry, TU Wien, Austria; Tomohiro Tachi, tachi@idea.c.u-tokyo.ac.jp, Department of Architecture, University of Tokyo, Japan; Kiumars Sharifmoghaddam, kiumars.sharifmoghaddam@tuwien.ac.at, Inst. of Discr. Math. and Geometry, TU Wien, Austria.

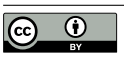


ACM 1557-7368/2025/12-ART235
https://doi.org/10.1145/3763808

**ACM Reference Format:**
Felix Dellinger, Martin Kilian, Munkyun Lee, Christian Müller, Georg Nawratil, Tomohiro Tachi, and Kiumars Sharifmoghaddam. 2025. Snapping Deployable Toroids for Modular Gridshells. *ACM Trans. Graph.* 44, 6, Article 235 (December 2025), 21 pages. https://doi.org/10.1145/3763808

## 1 Introduction

The construction of doubly curved surfaces has long been a central challenge in architectural geometry, especially when targeting lightweight, buildable, and geometrically controlled forms. While traditional approaches often rely on tiling such surfaces with repeatable components, our focus shifts toward assembling shell structures from modules that are individually tailored to the geometry. This approach offers greater design flexibility and curvature resolution, enabling structurally expressive forms that go beyond conventional repetition.

Deployable structures have emerged as a compelling solution in this context, enabling spatial systems that can fold, compress to enhance the transportability, or transform to suit a variety of functional and environmental demands. Origami, in particular, has proven to be a powerful functional design strategy, offering a rich geometric vocabulary for folding mechanisms that embed both structure and motion. Beyond its visual appeal, origami provides a precise geometric framework for shaping surfaces, enabling localized movements and coordinated global transformations, particularly when extended into three-dimensional configurations.

Origami structures can broadly be classified into *rigid* and *non-rigid* systems. In rigid origami, the faces are assumed to be non-deformable panels connected via ideal hinges, allowing the structure to fold without stretching or bending any surface elements. This property is especially useful for applications involving thick materials or precise kinematic control. Non-rigid origami, on the other hand, permits elastic deformation of panels and/or hinges during motion, which enables a wider range of transformations, but introduces mechanical complexity. In the latter case, recent interest has focused on structures that exhibit *multistability*. This is the ability to stably hold multiple configurations, often realized through geometric frustration or elastic snap-through behavior. Such multistable systems have been explored for their potential in shape morphing, mechanical memory, and deployable mechanisms. Our work builds on this foundation by developing bistable origami modules that are individually flat-foldable, geometrically programmable, and capable of tessellating curved surfaces.

### 1.1 Contribution and overview

This paper presents a geometric investigation into a new class of deployable, snapping origami toroids, which we term *PQ-toroids*. Our work builds upon the framework established in [Lee et al. 2024], where *T-toroids* are introduced as a class of multistable origami modules derived from T-hedral tubes. These T-toroids were shown to be flat-foldable and could be assembled into positively curved surfaces. However, as discussed in [Lee et al. 2024, Sec. 3], the design space of T-toroid assemblies is *limited to convex geometries*, significantly restricting their architectural potential.

In contrast, the *PQ-toroids* introduced in this work offer a substantially broader design space. While retaining multistability and deployability, they impose far fewer geometric constraints. In Section 2 we show how a PQ-toroid can be constructed from a general hexahedron with planar faces where the top and the bottom face are parallel.

Consequently, PQ-toroids conform to any quadrilateral mesh with planar faces and coplanar offset directions. We show in Section 3 how this allows us to approximate any given surface with a PQ-toroid tessellation.

Mechanically, PQ-toroids are bistable: they exhibit a zero-energy flat state and a deployed state, with the transition involving elastic deformation of material and a characteristic *snapping behavior*, analyzed in detail in Section 4. Their infinitesimal flexibility is discussed in Section 2.4.

As a demonstration, we fabricated a desktop-scale structure composed of sixty PQ-toroids. Each module can be folded flat by pressing two opposite sides inward and can snap back to its deployed form via gentle tension (see the supplemental videos).

We discuss the design pipeline which allows for surface-guided module generation and give more digital examples in Section 5. We conclude with a discussion of the limitations in Section 6.

### 1.2 Previous and related work

#### 1.2.1 *On the conceptual level.*

*Deployable structures.* Deployable structures are spatial systems that can transition between compact and expanded configurations, typically for the purposes of storage, transport, or on-demand deployment. They have long been of interest in aerospace, architecture, and civil engineering. Early innovations in the field include Hoberman's mechanical linkages and expandable domes [Hoberman 1990]. With a similar mechanism, Ren et al. [2022] introduce a bistable structure that deploys into a surface with structural thickness. Pioneering structural studies by Guest and Pellegrino established theoretical models for deployability, structural stiffness, and transformability in large-scale systems, including in Guest's doctoral work [Guest 1994] and in Pellegrino's monograph *Deployable Structures* [Pellegrino 2001].

More recently, origami has been adopted as a geometric framework for deployable structures, particularly in architectural contexts, offering both material efficiency and precise control over form. Some notable works include the development of Miura-ori–based foldable shelters [Curletto and Gambarotta 2016; Thrall and Quaglia 2014], rigid-foldable canopy [Ando et al. 2020], thick-panel deployables [Zhu and Filipov 2024], and mechanisms incorporating snap-through behavior [Melancon et al. 2021]. These systems leverage folding kinematics to achieve deployability without the need for traditional mechanical joints, making them lightweight and fabrication-friendly. Our work builds on this trajectory, introducing multistable modules that combine geometric deployability with architectural curvature and modularity.

*Modular systems.* Having a system of prefabricated modules can bring considerable advantages such as faster, safer and more precise manufacturing and construction as well as having lower environmental impacts [Thai et al. 2020]. Architectural modularity enables the discretization of complex surfaces into constructible units, which may vary locally to conform to curvature and structural requirements. In computational design, modularity allows curvature

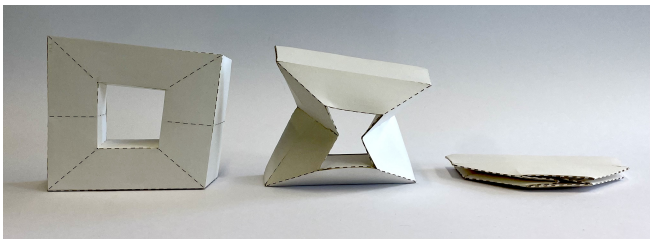

Fig. 2. Flat-folding of a deployed toroid. *Left to right:* PQ-toroids number 18, 4 and 14 of the desktop model illustrated in Figure 20 in fully deployed, half-folded and flat-folded states. The deployed and flat-folded states have planar faces with zero stored energy, while the unstable half-folded state in the middle exhibits deformation of the faces.

approximation using deployable [Wei and Pellegrino 2017], volumetric [Bechert et al. 2021] or panel-based [Eigensatz et al. 2010; Pottmann et al. 2007a] primitives.

*Lightweight gridshells.* Doubly curved shell structures benefit from lightweight, deployable, and tessellated design strategies. Such systems minimize material use while offering expressive spatial performance. While many recent works on deployable lightweight gridshells consider elastic or active bending structures [Lienhard et al. 2013; Lienhard and Gengnagel 2018; Panetta et al. 2019; Pillwein and Musialski 2021], in our work we demonstrate how snapping origami modules can realize curved surfaces in deployable architecture.

*Rigid and non-rigid origami.* Rigid origami assumes panels remain undeformed during motion, allowing analytical modeling and structural predictability. Kinematics and geometry of rigid origami as well as its folding simulation have been studied widely, pioneered by the works of Tachi et. al [2009b; 2011]. Non-rigid origami relaxes this constraint, introducing elastic deformations and enabling multistable behavior [Liu et al. 2021]. The work of Liu and Paulino [2017] and Bertoldi et al. [2017] establishes multistability as a design feature, rather than a byproduct, with applications in shape morphing and structural reconfiguration.

#### 1.2.2 *On the module level.*

*Non-Euclidean origami.* conventional applications of origami in engineering [Koryo 1985] often consider a fully developable sheet to start the folding process. This is not only an inspiration from the art of paper folding, but rather a fabrication and manufacturing choice due to the thin materials often being produced in sheets. Towards recent years, and along with the advances in additive manufacturing, this paradigm has shifted and non-developable yet flat-foldable systems [Tachi 2009a] capable of embedding negative or variable Gaussian curvature have drawn interest and have been studied from a geometric and kinematic point of view [Foschi et al. 2022; Waitukaitis et al. 2020].

*Tubular origami.* Miura-ori pattern and its tubular variants [Filipov et al. 2015; Tachi and Miura 2012] form the geometric core of several recent multistable tubular origami structures [Fang et al. 2017; Wang et al. 2024; Yasuda and Yang 2015]. An approach based on Monge surfaces and so-called cone nets was taken by [Vidulis et al. 2025] to obtain 3D tubular structures composed of developable surface strips. Sharifmoghaddam et al. [2023] presented a generalization of rigidly foldable origami tubes to T-hedral [Sharifmoghaddam et al. 2020] design space. Based on that, Lee et al. [2024] introduced multistable T-toroids for constructing positively curved surfaces.

*Multistability analysis.* The multistable origami modules are often analyzed to understand their interesting behavior, such as snapping transition, shape stability, using the geometric or mechanics perspective. Jianguo et al. [2015] modeled bistable origami as the bar elements and estimated the energy barrier by bar stretch, and Melancon et al. [2021] and Lee et al. [2023] estimated the energy barrier as a metric for the incompatibility between multiple rigid origami. Mechanics-based analysis of multistable origami modules often uses a bar-and-hinge model-based snap-through energy computation, finite element analysis, and experimental validation. Filipov and Redoutey [2018], also Liu et al. [2019] analyzed metastable transitions using the experiments and bar-and-hinge model, and Almessabi et al. [2024] analyzed reprogrammable multistable origami modules using finite element analysis and experiments. These form the background of the analysis methods of geometry and mechanics for the bistable behavior studied in this paper. Beyond the methods discussed above, [Chen et al. 2021] analyzes deployment energy barriers and stiffnesses of a bistable deployable material system around the deployed state using a finite element numerical homogenization approach.

#### 1.2.3 *On the surface level.*

*Discrete conjugate nets and offset meshes.* PQ-toroid structures are typically materializing two layers of quad meshes where each quad is planar. Such nets are well studied in discrete differential geometry under the name 'conjugate net' or Q-nets. Already Sauer [1970] defined discrete conjugate nets as quad nets with $\mathbb{Z}^2$ combinatorics such that each quad is planar. Smooth conjugate nets have been studied extensively with respect to transformation theories in the last two centuries. Bobenko and Suris [2008] have laid the ground for discretizing this transformation theory in a systematic way. Q-nets, in particular if they follow principal directions on the surface, have become increasingly important in applications. They appear within multilayer structures to control 'thickness' of a mesh (as our toroidal structures do) in [Liu et al. 2006; Pottmann et al. 2015, 2007b]. The offset mesh is also important for the snapping property of the toroids. Also of interest are special offset properties like face-offset and edge-offset properties [Pottmann et al. 2010, 2007b].

## 2 Snapping Toroids

We are aiming for discrete toroidal structures that can snap between two stable states; namely a flat-folded one and a deployed state. Note that the existence of a flat state in combination with the *Bellows Theorem* [Connelly et al. 1997] implies rigidity of the toroidal structure. However, we design our toroids such that they become rigid foldable tubes after one cut, see Figure 7. On the one hand, this ensures that every corner is flat-foldable (compare Theorem 2.1), and on the other hand, it provides a useful design tool to construct a globally flat-folded state. Moreover, the rigid movement of the cut open parts of the toroid allows us to precisely measure the gap that

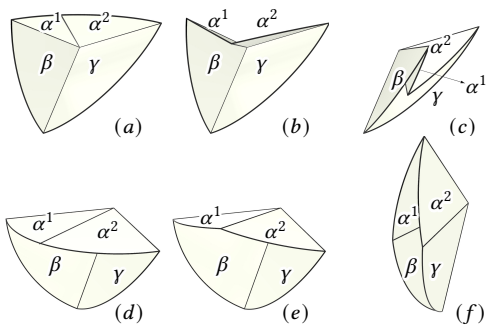


Fig. 3. *Top:* A non-developable degree-4 vertex, $(a)$ in a singular configuration, where a dihedral angle (between $\alpha^1$ and $\alpha^2$) is zero, $(b)$ a valley fold is introduced, and $(c)$ close to a flat-folded state demonstrating $\alpha^1 - \alpha^2 + \gamma - \beta = 0$. *Bottom:* Similar degree-4 vertex, $(d)$ in a singular configuration, $(e)$ a mountain fold is introduced, and $(f)$ close to a flat-folded state demonstrating $\alpha^1 - \alpha^2 - \gamma + \beta = 0$.

has to be closed through material deformation, see Section 4.1 for details.

This idea was already used in [Lee et al. 2024] where the authors introduced the so-called T-toroids. The foldable tube closing up to form a T-toroid is of the T-hedral type described in [Sharifmoghaddam et al. 2020]. Although the high symmetry of these tubes makes them attractive for manufacturing, we will see in Section 3 that the design space of T-toroid-only structures satisfying the assembly conditions given in [Lee et al. 2024] is limited to convex shapes discretized by edge-offset-meshes.

Consequently, we need to base our toroids on a more general flexible tube. In Section 2.1, we show that such a tube can be carved out from a hexahedron with planar faces and parallel top and bottom face, a *PQ-hexahedron* (see Fig. 4). This allows for a wide variety of shapes as basically any surface can be approximated by a grid shell of PQ-hexahedra; see Section 3.

In general, the tube carved out from a PQ-hexahedron does not close in its flat state. We show in Section 2.2 that this can be achieved by adding two extra foldlines. The shape space of PQ-hexahedra is 9-dimensional if one cancels out similarities by fixing one side of the hexahedra. The final T-toroid is then uniquely determined by two more parameters: the width $W$ of the parallelogramic cross-section of one side of the toroid and one parameter $\theta$ for the position of the extra foldlines. Hence, the class of the resulting PQ-toroids is 11-dimensional.

## 2.1 Geometric construction implied by local flat-foldability

We consider a hexahedron with planar faces, where the top and bottom face are parallel and refer to it as a PQ-hexahedron; compare Fig. 4. We show that a locally flat-foldable toroid with parallelogramic cross-section can be carved out of this hexahedron with exactly one degree of freedom.

By having parallelogramic cross-section, the toroid can be cut in four prisms that each flat fold with one degree of freedom. For the entire tube to flat fold, an adapted version of the *Kawasaki's theorem* [Foschi et al. 2022] has to hold:

Theorem 2.1. *Let $\alpha^1, \alpha^2, \gamma$ and $\beta$ be the angles of a flat-foldable corner in a PQ-toroid, like in Fig. 3$(a)$. Then either $\beta - \alpha^1 = \gamma - \alpha^2$ (valley fold; Fig. 3$(c)$) or $\beta + \alpha^1 = \gamma + \alpha^2$ (mountain fold; Fig. 3$(f)$) has to hold.*

Therefore, the angles $\alpha_i, \beta_i, \gamma_i$ in a corner of the top face of the hexahedron (compare Fig. 4) already determine the angles $\alpha_i^1$ and $\alpha_i^2$ of the PQ-toroid by

$$\alpha_i^1 = \frac{\alpha_i \pm \beta_i \mp \gamma_i}{2} \quad \text{and} \quad \alpha_i^2 = \frac{\alpha_i \mp \beta_i \pm \gamma_i}{2}. \tag{1}$$

The choice of sign determines whether the foldline is a mountain fold or a valley fold, which has to be consistent throughout the toroid. Due to the edge parallelity of top and bottom face, the angles at the bottom corner are $\alpha_i, \pi - \beta_i, \pi - \gamma_i$. Thus, we obtain coplanar foldlines for the bottom corner with the same angles $\alpha_i^1$ and $\alpha_i^2$. A valley fold angle in the top corner corresponds to a mountain fold angle in the bottom corner, and vice versa.

With the foldlines prescribed, the toroid seems overdetermined as the width $W_i$ of one prismatic tube determines the width $W_{i+1}$ of the next tube by

$$W_{i+1} = W_i \frac{\sin \alpha_{i+1}^1}{\sin \alpha_{i+1}^2}. \tag{2}$$

However, the next lemma shows that the angles $\alpha_i^1$ and $\alpha_i^2$ meet a loop-closure condition.

Lemma 2.2. *The angles $\alpha_i^1$ and $\alpha_i^2, i \in \{0, \dots, 3\}$ determined by Kawasaki's theorem in a PQ-hexahedron naturally meet the loop-closure condition*

$$\prod_{i=0}^{3} \frac{\sin \alpha_i^1}{\sin \alpha_{i+1}^2} = 1 \tag{3}$$

*with all indices taken modulo* 4.

Proof. We give a geometric reason why the above formula holds. Assume that we have a valley fold at the top corners, i.e. $\alpha_i^1 = (\alpha_i + \beta_i - \gamma_i)/2$ and $\alpha_i^2 = (\alpha_i - \beta_i + \gamma_i)/2$. Then, the foldlines are also the lines along which a sphere $S$, tangent to the two side faces and the top face, touches the top face. This is due to the fact that the touching points of $S$ form equal angles with the edges of the hexahedron, compare Fig. 5. We can assume that all side faces of the PQ-hexahedron touch the same sphere $S$, since the loop-closure condition is not affected by parallel translation of the side faces. This implies that all foldlines meet at a single point forming four triangles. In this configuration the loop-closure condition is obviously met and thus it is met in the original PQ-hexahedron as well. Switching from valley folds to mountain folds only exchanges the role of $\alpha_i^1$ and $\alpha_i^2$. Consequently, the loop-closure condition holds in the case of mountain folds as well. □

## 2.2 Extra foldlines for global flat-foldability

So far, we have only taken care of the local foldability of the PQ-toroid. The existence of the global flat state is achieved by adding two extra foldlines. To do this, we cut the PQ-toroid open through the foldlines at corner zero and compute the flat-folded tube. Let us

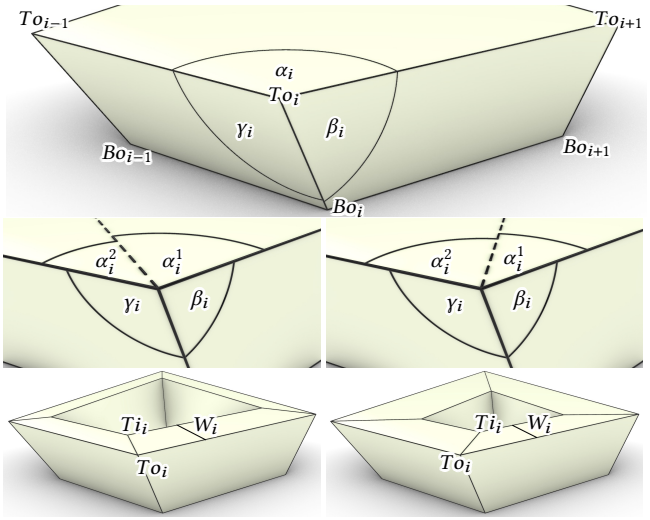


Fig. 4. *Top:* A PQ hexahedron. We denote the angles at the top corner $To_i$ by $\alpha_i, \beta_i$ and $\gamma_i$. *Center:* The Kawasaki theorem determines the foldlines in the corners. *Left:* We see the foldline of a mountain fold, and *right:* we see the one of a valley fold. *Bottom:* The PQ-hexahedron can be carved out along the foldlines yielding the inner vertices $Ti_i$ in the top faces and $Bi_i$ at the bottom faces. Due to Lemma 2.2 all faces are trapezoids. The *left* toroid corresponds to a mountain fold in the top faces and *right* to a valley fold.

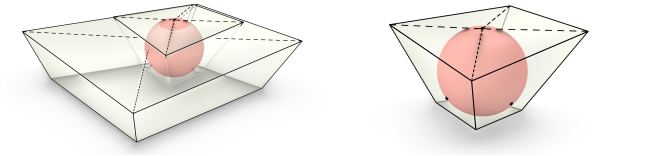

Fig. 5. *Left:* For every PQ-hexahedron we can find a PQ-hexahedron with parallel faces and edges such that all faces touch a common sphere. *Right:* If all faces of a PQ-hexahedron touch a common sphere, then the valley foldlines intersect in the touching point of that sphere. From this, it is easy to see that the angles have to meet equation (3).

denote the flat vertices by $Bo^*, To^*, Bi^*, Ti^*$. They are recursively given by

$$X^*_{i+1} = X^*_i + \begin{pmatrix}\cos(\delta_{i+1})\\ \sin(\delta_{i+1})\end{pmatrix} \|X_{i+1} - X_i\|,$$

$$\delta_{i+1} = \delta_i + (-1)^i \cdot (\pi - \gamma_i + \beta_i), \quad \delta_1 = 0$$

$$Bo^*_0 = \begin{pmatrix}0\\0\end{pmatrix}, \; Bi^*_0 = \begin{pmatrix}\cos(\alpha^1_0)\\ \sin(\alpha^1_0)\end{pmatrix} \|Bi_0 - Bo_0\|,$$

$$To^*_0 = \begin{pmatrix}\cos(\pi - \beta_0)\\ \sin(\pi - \beta_0)\end{pmatrix} \|To_0 - Bo_0\|, \; Ti^*_0 = Bi^*_0 + To^*_0,$$

where $X \in \{Bo, To, Bi, Ti\}$ and $i \in \{0, 1, 2, 3\}$. Note that in this case $X^*_4 \neq X^*_0$. Instead, we obtain two congruent quadrilaterals $[Bo^*_0, To^*_0, Ti^*_0, Bi^*_0]$ and $[Bo^*_4, To^*_4, Ti^*_4, Bi^*_4]$, compare Fig. 7. Since they have the same orientation they are related by a rotation of angle $\phi$ around center $c$. This rotation is the composition of the reflections across two lines intersecting at $c$, forming the angle $\phi/2$. Hence, the first foldline is computed by intersecting a line through $c$ in direction $(\cos(\theta), \sin(\theta))^T$ with the four segments $X^*_k X^*_{k+1}$, $X \in \{Bo, To, Ti, Bi\}$. The intersection points are then mapped back to the deployed state. For the second fold we rotate the previous line around $c$ by the angle $-\phi/2$ and intersect the segments $X^*_l X^*_{l+1}$, $X \in \{Bo, To, Ti, Bi\}$ where $l > k$. The change of sign in the angle is due to the fact that the second foldline is reflected in the first foldline as well.

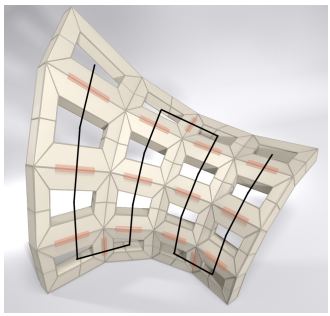

Fig. 6. The toroids sharing a colored edge can stay connected while they are flat folded. By adding the extra fold lines on opposite and adjacent edges of the toroids one can connect the entire structure. The black path demonstrates the connectivity of the structure.

The free parameter $\theta$ can be tedious in the design process as it has to be chosen for every toroid. As an initial choice we simply aim to put the extra foldlines as close to the center of the intersected edges as possible. To do so, we enumerate the eight edges that are intersected by the extra foldlines and denote the ratio with which the $i$-th edge is divided by $\lambda_i$. The concave function $f(\theta) = \sum_{i=1}^{8} \lambda_i(1 - \lambda_i)$ gives a measure on how centered the foldlines are. Choosing $\theta$ as the maximizer of $f$ gives a geometrically reasonable placement for the extra foldlines. Starting from this initial choice a more sophisticated placement of the foldlines can then be done by taking the analysis of Section 2.4 and 4 into account.

Apart from choosing $\theta$, one also has to choose which edges to intersect. This can affect the collision behavior of the toroid. We distinguish three cases. If the sum of lengths of inwards folding edges is smaller than the length of the edge they fold towards, then no collision can appear during the folding motion. If one of the inward folding edges is longer than the edge it folds towards, then the flat state will always have self-intersection. For the cases in between, collisions can occur during the folding motion. However, if one allows the faces to slide on top of each other, the folding motion is still possible. This sliding motion was observed in all physical models in which collisions occurred.

Toroids that share an edge without extra foldline can stay connected during their folding motions. By correctly placing additional foldlines, the user can create arbitrarily large regions that flat fold simultaneously, compare Fig. 6.

## 2.3 The special case of T-toroids

The afore mentioned T-toroids introduced in [Lee et al. 2024] appear as a special case of PQ-toroids. T-toroids can be generated by two planar polygons $P$ and $T$ on two orthogonal planes. The profile polygon $P$ is then swept along the trajectory polygon $T$ from one bisector plane of consecutive edges of $T$ to the next one. If the trajectory is a quad and the profile is a parallelogram with a pair of opposite sides parallel to the base plane containing $T$, then it is a

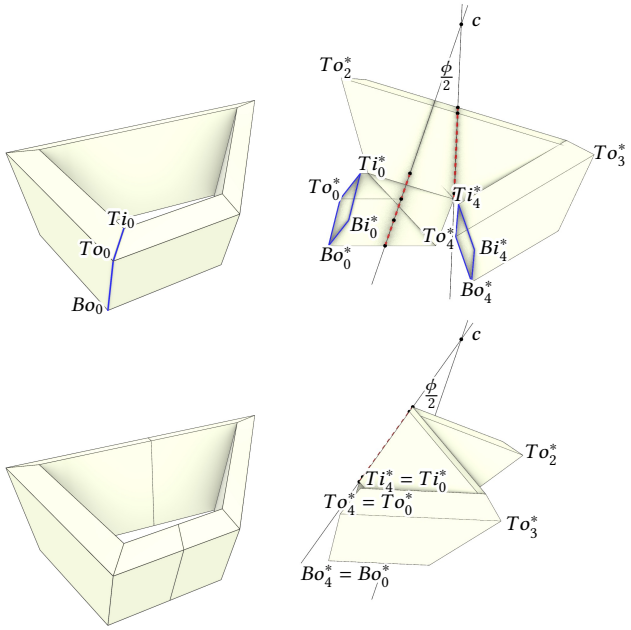


Fig. 7. *Top left:* We start with a PQ-toroid without extra foldlines, and cut it open to a tube. *Top right:* The resulting tube is flat-foldable but in the flat state the ends do not close. The two open ends illustrated in blue can be mapped onto each other by two reflections. The intersection of these reflection lines give the extra foldlines indicated by dotted red points. *Bottom right:* Folding the toroid along these dotted red lines closes the flat tube. *Bottom left:* Going back to the deployed state, we obtain the final PQ-toroid.

special case of a PQ-toroid (see Fig. 8). Similarly, if a PQ-toroid has the additional property that $\alpha_i^1 = \alpha_i^2$ for all $i$, it is a T-toroid.

Since $\alpha_i^1 = \alpha_i^2$ the parallelogramic cross-section in a T-toroid has constant width. All side faces of a T-toroid have the same height and form the same angle with the base plane. Moreover, $\gamma_i = \beta_i$ in every corner of the T-toroid. In a T-toroid grid-shell this property of equal angles propagates around a vertex star. Hence, the edges of the underlying mesh are contained in one side of a rotational cone per vertex star. In particular, this implies that every vertex star is positively curved and thus T-toroid grid-shells can only form convex structures.

Since the inner foldlines in the corners of a T-toroid are the angle bisectors, all corners can be mountain and valley folds at the same time. This implies a bifurcation that allows for two modes of folding. We analyze the snapping behavior of these two modes in Section 4.

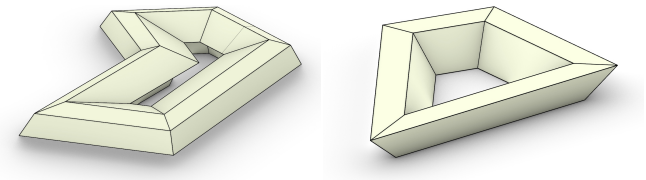

Fig. 8. *Left:* A general T-toroid generated by arbitrary profile and trajectory polygons. *Right:* A T-toroid with parallelogram-based cross-section and quadrilateral trajectory is a special case of a PQ-toroid. Due to its symmetry the corner foldlines can be all either with mountain or valley assignment.

## 2.4 Infinitesimal flexibility analysis

It can easily be seen that a PQ-toroid without additional foldlines in its deployed state only allows the infinitesimal translation of the inner ring in the $z$-direction under the assumption that the outer ring (which is in general rigid[1]) is fixed to the reference frame in a way that the top and bottom faces are parallel to the $xy$-plane.

Now the question arises if the deployed structure obtains additional infinitesimal flexes by adding the extra foldlines? One way to check this would be to compute the kernel of the rigidity matrix [Schulze and Whiteley 2017], which would be in this case a $96 \times 66$ matrix[2]. In the following, we use a tailor-made approach which simplifies computation and gives us a first criterion for the selection of the additional foldlines.

We consider again the inner and the outer ring of the toroid consisting of six panels. Now both rings can be considered as closed kinematic 6R chains, i.e. two adjacent panels are connected by a rotary (R) joint. Each of these 6R loops is infinitesimally flexible as the six rotation axes belong to a singular[3] linear line complex [Pottmann and Wallner 2001, Sec. 3.1]. One can compute the corresponding infinitesimal flex of each 6R loop, which is determined by the ratio of angular velocities of the axes $O_1, \ldots, O_6$ of the outer 6R loop and of the axes $I_1, \ldots, I_6$ of the inner one, respectively. In general[4] these two infinitesimal flexes of the 6R loops do not fit together to imply an additional degree of freedom on the level of velocities to the toroid; beside the already mentioned infinitesimal translation of the inner ring to the outer one. The closeness of the structure to such an additional infinitesimal flexibility can be evaluated kinematically as explained in Appendix A.

In contrast to the deployed state, the flat-folded toroid starts deploying along an infinitesimal flex. The existence of this flex follows already from the fact that all edges are coplanar. Therefore, the velocity vectors of the vertices are orthogonal to this plane, and will not change the lengths of the edges in first order. This shows that the flat-folded state is not stiff in contrast to the deployed one. The above mentioned closeness index can be interpreted as stiffness (see Appendix A), which can serve as a design criterion; e.g. for the selection of the additional foldlines.

# 3 Surface and Shape Generation

## 3.1 Modules to meshes

We start by geometrically assembling our modules into shell structures and derive properties for the underlying meshes. Our overarching goal is to approximate a given surface $\Phi$ by a grid of PQ-toroids

[1] It can only be infinitesimal flexible if the four edges of the outer ring belong to a bundle of lines, field of lines, a regulus or two pencils of lines, where the intersection line of the two carrier planes equals the line spanned by the two pencil vertices [Pottmann and Wallner 2001, Sec. 3.3].

[2] We have 96 edges (including both diagonals of each quad) and 24 vertices, which imply $24 \cdot 3 = 72$ variables, but 6 can be set to zero in order to eliminate rigid-body motions of the complete structure.

[3] The six axes are located in two planes and their common line equals the axis of the singular linear line complex.

[4] In special cases an additional flex can exist as demonstrated in Example 5.7.

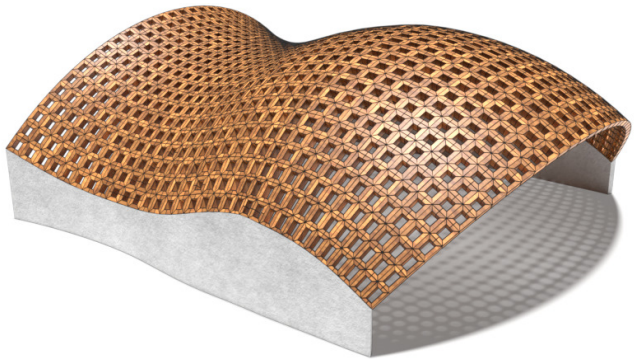

Fig. 9. Doubly curved surface with toroids. We optimized the base net for the Q-net property and additionally in the positively curved area for the edge-offset property and in the negatively curved area for the face-offset property. In this way the positively curved area is covered mainly with T-toroids and the negatively curved area with PQ-toroids. See also Sec. 3.2.1 and 3.2.2.

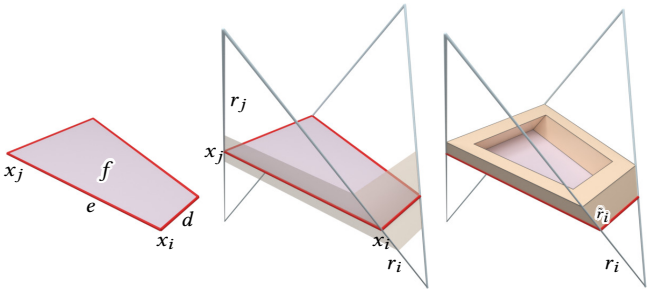


Fig. 10. Geometric properties of a PQ-toroid. *Left:* A planar quadrilateral face $f$. Two edges $e, d$ are emanating from vertex $x_i$. *Center:* Through each vertex $x_i$ there is a ruling $r_i$. Edge-neighboring rulings meet in a point. *Right:* The planes of the toroids coincide with the planes spanned by edge-neighboring rulings.

(see Sec. 3.3). More precisely, we will consider a surface mesh $\mathcal{M}$ which approximates $\Phi$ such that there is

(i) one toroid per face of the mesh,
(ii) for each face of the mesh the face itself is identical with the base quadrilateral of the corresponding toroid (Fig. 10 right),
(iii) neighboring toroids share a common toroid-face.

From (ii) follows that the faces of mesh $\mathcal{M}$ are planar quadrilaterals (hence, $\mathcal{M}$ is often called a *PQ-mesh*). If such a PQ-mesh has the combinatorics of a $\mathbb{Z}^2$ lattice it is called a *Q-net* or *(discrete) conjugate net*. These nets discretize smooth conjugate nets or conjugate parametrizations of a smooth surface (see, e.g., [Bobenko and Suris 2008; Doliwa and Santini 1997]). Illustrations of conjugate nets are depicted in Fig. 14: smooth (b) and discrete (f). We conclude:

Lemma 3.1. *Discrete parametrizations that are covered by PQ-toroidal structures are Q-nets.*

From (iii) follows that there is a unique plane $\varepsilon_e$ through each edge $e$ containing the side face of neighboring PQ-toroids. Consider two such planes $\varepsilon_e, \varepsilon_d$ corresponding to two edges $e, d$ emanating from a vertex $x_i$ in a face $f$ (see Fig. 10). These two planes contain two neighboring faces of the PQ-toroid and therefore intersect in an edge $\tilde{r}_i$ of the PQ-toroid. Since neighboring PQ-toroids share corresponding faces, all planes $\varepsilon_e$ around a vertex star pass through a common line $r_i$, a *ruling*, containing $\tilde{r}_i$. Two rulings $r_i, r_j$ corresponding to vertices $x_i, x_j$ which are connected by an edge $e$ must lie in the same plane $\varepsilon_e$ and therefore intersect in a point. This point could be a point at infinity since $r_i$ and $r_j$ could be parallel. We conclude:

Lemma 3.2. *PQ-toroidal structures come with rulings (straight lines) $r_i$ per vertex $x_i$. Edge-neighboring rulings $r_i, r_j$ intersect in a point (including points at infinity).*

A discrete two-parameter family ($\mathbb{Z}^2$ combinatorics) of straight lines where neighboring lines intersect is called a *discrete hyperbolic line congruence*. This term comes from smooth line geometry (see, e.g., [Pottmann and Wallner 2001, p. 427]).

We have discovered that the two notions, Q-nets and hyperbolic line congruences, are important for us. We will therefore derive both notions from within their smooth theory and give a short introduction for both.

*3.1.1 Conjugate nets (Q-nets).* Discrete nets with the combinatorics of a $\mathbb{Z}^2$ lattice and planar quadrilateral faces (PQ-meshes) discretize conjugate surface parametrizations (see, e.g., [Bobenko and Suris 2008, Def 1.1]).

Definition 3.1. *A parametrization of a surface $f: U \subset \mathbb{R}^2 \to \mathbb{R}^3$ is said to be* conjugate *or $f$ is a* conjugate net *or a* Q-net *if $\partial_{uv} f \perp n$ where $n$ is the unit normal vector field.*

Conjugate nets are invariant under projective transformations and should therefore be considered within the framework of projective differential geometry of which we refrain for the sake of simplicity. A detailed source on that topic is [Lane 1942].

Definition 3.2. *Let $f: U \to \mathbb{R}^3$ be a Q-net. A net $g: U \to \mathbb{R}^3$ is called* parallel to $f$ *or a* Combescure transform of $f$ *if $\partial_u f \parallel \partial_u g$ and $\partial_v f \parallel \partial_v g$ everywhere (see, e.g., [Bobenko and Suris 2008, Def 1.4]).*

The existence of a non-trivial Combescure transform characterizes Q-nets. We will need the notion of Combescure transforms to characterize all hyperbolic line congruences in Section 3.1.2.

*Example* 3.3. A curvature line parametrization $f$ (cf. Bobenko and Suris [2008, Sec. 1.4.4]) of a smooth surface is conjugate. Any offset $f^d = f + dn$ of a principal curvature parametrization with $d \in \mathbb{R}$ is also conjugate and a Combescure transform of $f$.

Discrete Combescure transforms $g$ of discrete Q-nets $f: U \subset \mathbb{Z}^2 \to \mathbb{R}^3$ are edgewise parallel, i.e., $f_i - f_j \parallel g_i - g_j$ for all pairs of neighboring vertices $(x_i, x_j)$. Consequently, a toroid structure consists of a pair of Q-nets which are Combescure transforms of each other.

*3.1.2 Smooth line geometry.* Line congruences belong to the field of *line geometry*. A detailed source on this topic is [Pottmann and Wallner 2001]. In this section, we will recall only a few necessary concepts.

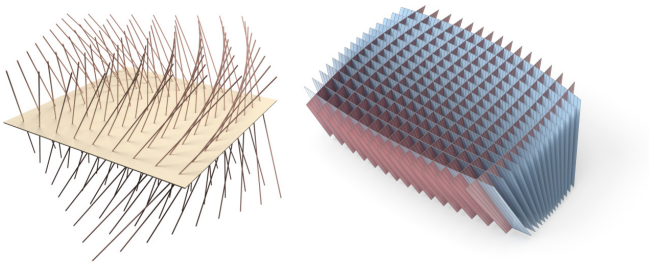

Fig. 11. *Left:* Elliptic line congruence. Any congruence surface, i.e., one-parameter subfamily of lines, forms a *skew* ruled surface. *Right:* Hyperbolic line congruence. Through each ruling of the congruence there are two congruence surfaces that are *torsal* ruled surfaces.

Definition 3.4. *A* line congruence $\Gamma$ *is a two-parameter family of straight lines (*rulings*).*

A line congruence $\Gamma$ can be parametrized by

$$c(u, v, \lambda) = f(u, v) + \lambda r(u, v),$$

where $f\colon U \subset \mathbb{R}^2 \to \mathbb{R}^3$ parametrizes a *reference surface* and $r\colon U \to \mathbb{R}^3 \setminus \{0\}$ a vector field. The parameter of the ruling is $\lambda$. A *congruence surface* is a ruled surface generated from a one-parameter subfamily of a given line congruence. They can be represented in the form $c(u(t), v(t), \lambda)$ for some curve $\varphi(t) = (u(t), v(t))$ in the parameter domain. Such a congruence surface can be *torsal* (i.e., developable) or *skew* (i.e., non-developable).

Definition 3.5. *A line congruence* $\Gamma$ *is called* hyperbolic [parabolic, elliptic, torsal] *if in each ruling* $r$ *of* $\Gamma$ *there are exactly 2 [1, 0, $\infty$] torsal congruence surfaces passing through* $r$*. See, e.g., [Pottmann and Wallner 2001, Sec. 7.1] and for an illustration see Fig. 11.*

*Example* 3.6. A simple example of a congruence is obtained by connecting each point of a reference surface with a single point (a *vertex*). In this way, we generate a part of a *line bundle*. This line congruence has the form

$$c = (1 - \lambda)f + \lambda p \quad \text{or} \quad c = f + \lambda q,$$

if the point $p$ is a finite point in $\mathbb{R}^3$ or if the vertex is a point at infinity in direction $q$, respectively.

*Example* 3.7. An important example of a line congruence is the *normal congruence* consisting of all normals of a smooth surface $\Phi$. The surface normals along a curve $\gamma$ on $\Phi$ are torsal if and only if $\gamma$ is a curvature line. Since every smooth surface has two curvature lines passing through each point, the normal congruence of a generic surface is hyperbolic.

In a hyperbolic line congruence $\Gamma$ we have two families of torsal congruence surfaces. These congruence surfaces can be aligned with a conjugate parametrization of the reference surface $\Phi$ in the following sense (cf. [Lane 1942]).

Definition 3.8. *Let* $f(u, v)$ *be a Q-net on* $\Phi$ *and let* $\Gamma$ *be a hyperbolic congruence. Then* $\Gamma$ *and* $f$ *are called* conjugate *if the congruence surfaces* $u \mapsto c(u, v_0, \mathbb{R})$ *and* $v \mapsto c(u_0, v, \mathbb{R})$ *are the torsal congruence surfaces for all* $u_0, v_0$*.*

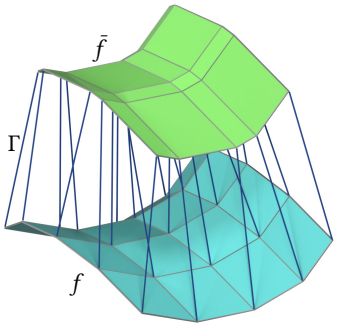


Fig. 12. Discrete Q-net with conjugate line congruence. The blue base net $f$ is a Q-net (planar quadrilateral faces and $\mathbb{Z}^2$ combinatorics). The Combescure transform $\bar{F}$ has corresponding parallel edges and faces. The lines connecting corresponding lines forms a discrete hyperbolic line congruence $\Gamma$. The congruence surfaces along the parameter lines are torsal.

Hence we conclude the following important observation: A pair $(f, \Gamma)$ consisting of a Q-net $f$ and a hyperbolic line congruence $\Gamma$ conjugate to $f$ is the smooth analogue to the discrete parametrization from Lemma 3.1 and the rulings from Lemma 3.2.

Lemma 3.3. *Let* $f$ *be a Q-net. Then all line congruences* $\Gamma$ *conjugate to* $f$ *are of the form*

$$c(u, v, \lambda) = (1 - \lambda)f(u, v) + \lambda \bar{f}(u, v),$$

*where* $\bar{f}$ *is a Combescure transform of* $f$*.*

In other words, all line congruences $\Gamma$ conjugate to a Q-net $f$ connect corresponding points of $f$ with a Combescure transform $\bar{f}$ of $f$. See Fig. 12 for an example of a discrete congruence conjugate to a discrete Q-net. This insight gives an intuitive method of designing a conjugate line congruence to a given Q-net.

We describe an application where a carefully placed Combescure transform generates a useful hyperbolic congruence in Example 5.4.

## 3.2 Meshes to modules

To obtain modules for a given mesh we must bring together discrete Q-nets with discrete hyperbolic line congruences. We start with a discrete version of Definition 3.8:

Definition 3.9. *Let* $f\colon U \subset \mathbb{Z}^2 \to \mathbb{R}^3$ *be a discrete Q-net and let* $\Gamma\colon U \to \{\text{lines in } \mathbb{R}^3\}$ *be a discrete hyperbolic congruence. Then* $\Gamma$ *and* $f$ *are called* conjugate *if edge-neighbouring lines are coplanar (hence generate a discrete torsal congruence surface). See Fig. 12.*

We are dealing with two different types of modules, PQ-toroids and T-toroids. A discrete conjugate pair consisting of a Q-net $f$ and a hyperbolic congruence $\Gamma$ (Def. 3.9) must have different properties to facilitate different types of toroids. While using T-toroids implies the usage of more special Q-nets as base surfaces (see Sec. 3.2.1), PQ-toroids are more flexible as every Q-net can be tessellated with PQ-toroids.

*3.2.1 T-toroids and edge-offset meshes.* As mentioned in Section 2.3 T-toroids have the properties that all side faces are trapezoids of equal height. Moreover, the "torsal" (i.e., vertical) ruling $r$ is the axis of a cone containing the adjacent edges $e_1, \ldots, e_4$ (see Fig. 13). These observations are summed up in the following lemma.

Lemma 3.4. *All edges of a vertex star of a Q-net that correspond to a conjugate pair* $(Q, \Gamma)$ *tessellated with T-toroids lie on a rotational cone whose axis is the corresponding ruling* $r$ *of* $\Gamma$*. Such a Q-net is a positively curved edge-offset mesh (Def 3.10).*

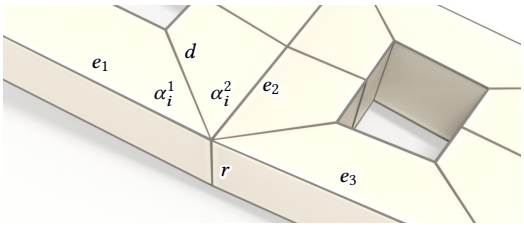


Fig. 13. Two neighboring toroids. The amount by "how much" the fold line $d$ deviates from the bisector of the edges $e_1$ and $e_2$ is governed by Eq. (1). Also the thickness of the toroid is more evenly distributed if the corner foldlines $d$ are close to those bisectors. Both depend on "how much" the ruling $r$ is a discrete normal (see Sec. 3.2.3).

Definition 3.10. *An* edge-offset *mesh is a PQ-mesh where there exists a non-trivial edge-wise parallel mesh such that corresponding edges have constant distance (see, e.g., [Pottmann et al. 2007a]).*

Edge-offset meshes are Laguerre isothermic surface parametrizations and as such objects of Laguerre geometry [Pottmann et al. 2010]. They are edgewise parallel to a Koebe polyhedron, which is a polyhedron whose edges touch a sphere.

*3.2.2 PQ-toroids and face-offset meshes.* For applications, a constant height between the two layers of the toroid structure might be a desirable property. This can be achieved if the two layers are face-offsets of each other.

Definition 3.11. *A* face-offset *mesh is a PQ-mesh where there exists a non-trivial edge-wise parallel mesh such that corresponding faces have constant distance (see, e.g., [Pottmann et al. 2007a]).*

Face-offset meshes are characterized by the existence of a cone of revolution at each vertex which is in tangential contact with the faces around this vertex [Pottmann et al. 2007a]. Taking a face-offset mesh $f$ and as line congruence $\Gamma$ the cone axes yields a conjugate pair $(f, \Gamma)$ which leads to a PQ-toroid structure with constant height throughout the surface.

*3.2.3 Toroids from normal congruences.* Taking as line congruence a discrete normal congruence (e.g., from face-offsets, edge-offsets, vertex-offsets or any other sensible definition) is useful for several reasons. One of them is that the foldlines are "bisecting" the corner angle of the base net: In Fig. 13 the angle between $e_1$ and $d$ is approximately the same as the angle between $e_2$ and $d$. This follows from Equation (1): If the ruling is approximately orthogonal to the base face then the two angles $\beta_i$ and $\gamma_i$ are approximately equal. Consequently, Equation (1) implies that $\alpha_i^1 \approx \alpha_i^2 \approx \alpha/2$. Another advantage is that the thickness of a toroid on all four sides is more equal the closer the aforementioned foldlines are to the angle bisectors, since $d_{i+1}/d_i = \sin(\alpha_{i+1}^1)/\sin(\alpha_{i+1}^2)$ see Eq. (2).

## 3.3 Surface approximation and optimization

*3.3.1 Finding a base surface.* In theory, there are infinitely many smooth Q-nets on a smooth surface $\Phi$. Q-nets that are suitable for architectural applications often have (nearly) orthogonal parameter curves, hence constitute a principal net. Consequently, a typical task is to find a discrete principal net on a given reference surface that is represented as a dense triangle mesh. We do this in three steps. First, we estimate principal directions for each face of the mesh as described in [Rusinkiewicz 2004]. We smooth and integrate the obtained vector field using libigl's [Jacobson et al. 2018] implementation of [Bommes et al. 2009]. This results in a mesh with quadrilateral faces that are almost planar. We planarize the faces of this mesh by applying the form-finding method [Tang et al. 2014]. This method works efficiently when the involved constraints can be written as quadratic polynomials of the variables (which can be achieved by introducing auxiliary variables).

Let the mesh $\mathcal{M}$ be defined by a set $V = \{x_1 \ldots, x_{|V|}\}$ of vertices and a set $F = \{f_1, \ldots, f_{|F|}\}$ of faces. To optimize for *planarity of faces* we introduce unit length face normals $n_i$ as auxiliary variables for all faces $f_i$ of the mesh $\mathcal{M}$, i.e.,

$$\|n_i\|^2 = 1, \qquad \langle n_i, x_j - x_k \rangle = 0,$$

for all edges $(x_j, x_k) \in f_i$. The above conditions are implemented as soft constraints and contribute to the total energy by the term

$$E_{\text{FN}} = \sum_{i=1}^{|F|} \left[ \left( \langle n_i, n_i \rangle - 1 \right)^2 + \sum\nolimits_{(x_j, x_k) \in f_i} \langle n_i, x_j - x_k \rangle^2 \right].$$

Optimizing for the *face-offset* property yields conical meshes [Liu et al. 2006]. These are Q-nets such that around each vertex star the four faces are tangent to a rotational cone. We introduce unit-length vertex normals $r_i$ as auxiliary variables which act as cone axes. Faces are in tangential contact with a cone if the angle between face normals $n_j$ (that we already introduced for planarization purposes) and the vertex normals $r_i$ are constant, i.e.,

$$\langle r_i, n_j \rangle^2 = c_i^2,$$

for all normals $n_j$ where the corresponding face $f_j$ is incident to vertex $x_i$. The sign of the inner product[5] is not important since we are dealing with double cones. The above equations contribute to the total energy by

$$E_{\text{FO}} = \sum_{i=1}^{|V|} \left[ \left( \langle r_i, r_i \rangle - 1 \right)^2 + \sum\nolimits_{f_j \ni v_i} \left( \langle r_i, n_j \rangle^2 - c_i^2 \right)^2 \right].$$

For aesthetic reasons, one can choose to use T-Toroids in positively curved areas as they allow for toroids with constant width in the entire structure. This requires an underlying *edge-offset* mesh according to Lemma 3.4. Hence, the edges emanating from a vertex must be the rulings of a rotational cone. In analogy to the above, the edge vectors of incident edges have to make a constant angle with $r_i$. We express this condition[6] as

$$\langle r_i, x_i - x_j \rangle^2 = d_i^2 \|x_i - x_j\|^2.$$

As energy contribution we get

$$E_{\text{EO}} = \sum_{i=1}^{|V|} \left[ \left( \langle r_i, r_i \rangle - 1 \right)^2 + \sum\nolimits_{x_j \sim x_i} \left( \langle r_i, x_i - x_j \rangle^2 - d_i^2 \|x_i - x_j\|^2 \right)^2 \right].$$

While PQ-toroids work well for positively and negatively curved surfaces, T-toroids have a tapering shape and can only be used for positively curved surfaces. Consequently, in the case of the presence of both signs in the surface curvature we can adjust the energy we

[5] Vertex normals $r_i$ are initialized as averages of incident faces normals and we start with $c_i = (\sum_{x_j \sim x_i} |\langle r_i, n_j \rangle|)/\text{valence}(x_i)$.

[6] The $d_i$ are initialized just like $c_i$ but using unit edge vectors instead of face normals.

optimize for at each vertex star depending on its curvature. See Fig. 9 for an example.

*3.3.2 Finding a line congruence.* To optimize a discrete line congruence to be torsal along parameter lines, we require a planarity condition for neighboring rulings passing through the vertices of an edge $e = (x_i, x_j)$. We use

$$\langle r_i \times r_j, x_i - x_j \rangle = 0$$

and obtain the energy contribution

$$E_{\mathrm{LC}} = \sum\nolimits_{(x_i,x_j)\in E} \langle r_i \times r_j, x_i - x_j \rangle^2.$$

*3.3.3 Additional energies.* For successful surface approximation a proximity measure (closeness to a reference surface) is required. Our reference surfaces $\Phi$ are represented as dense triangle meshes and we measure distance via a point-to-plane distance in the following way. Let $x_i^*$ denote the closest point to $x_i$ on the reference surface and let $n_i^*$ be the surface normal at $x_i^*$. The distance is evaluated by

$$\mathrm{dist}(x_i, \Phi) = \langle x_i - x_i^*, n_i^* \rangle,$$

which measures the distance of $x_i$ to the tangent plane at the closest point. Measuring distance in this way allows the mesh $\mathcal{M}$ to slide on $\Phi$. To allow large deformations, the footpoints $x_i^*$ are recomputed after a fixed number of iterations. Proximity contributes to the total energy by

$$E_{\mathrm{PROX}} = \sum\nolimits_{i=1}^{|V|} \langle x_i - x_i^*, n_i^* \rangle^2.$$

Form-finding typically requires a fairness measure in addition to proximity to a target surface. For meshes with $\mathbb{Z}^2$ combinatorics let $y_1, \ldots, y_4$ be the neighbors of a vertex $x_i$ in clockwise order. Our fairness energy term is then given by

$$E_{\mathrm{FAIR}} = \sum\nolimits_{i=1}^{|V|} \left[ \|y_1 + y_3 - 2x_i\|^2 + \|y_2 + y_4 - 2x_i\|^2 \right].$$

At vertices with degree different from four, simple Laplacian smoothing is applied (not listed explicitly in the following formulas).

*3.3.4 Total energy and implementation details.* To compute the vertex positions $x_i$ and torsal directions $r_i$ we minimize the energy

$$E = \tau_1 E_{\mathrm{FO}} + \tau_2 E_{\mathrm{EO}} + \nu_1 E_{\mathrm{FN}} + \nu_2 E_{\mathrm{LC}} + \nu_3 E_{\mathrm{PROX}} + \nu_4 E_{\mathrm{FAIR}}.$$

As mentioned above, weights $\tau_1$ and $\tau_2$ for $E_{\mathrm{FO}}$ and $E_{\mathrm{EO}}$ are set inside the respective terms on a per-vertex basis depending on curvature. For a positively curved vertex star we set $(\tau_1, \tau_2) = (0, \nu)$ where at a negatively curved vertex star we set $(\tau_1, \tau_2) = (\nu, 0)$ for some $\nu > 0$. The resulting non-linear least squares problem is solved using the Levenberg-Marquardt Algorithm [Marquardt 1963]. Except for $\nu_3$ and $\nu_4$, weights are typically 1 or 0 to turn constraints on or off. We chose values for $\nu_3$ in the range $[0.1, 1]$. The fairness weight $\nu_4$ was chosen in the interval $[0, 0.1]$ (0 to turn fairness off). As we approach a solution fairness is reduced gradually down to $10^{-6}$. During optimization the mesh $\mathcal{M}$ is scaled to fit the unit box. The Levenberg-Marquardt Algorithm is implemented in Python. For the most complex example (Fig. 17) one iteration takes slightly less than 1 second on a 12th generation Core i7 processor.

## 4 Snapping Behavior Analysis

In Section 2, we guaranteed the PQ-toroids to have a deployed state and a flat-folded one. During deformation from one state to the other, the structure must overcome an energy barrier (i.e., a deformation energy peak), causing the structure to snap. For the design of the snapping toroid, the evaluation of this energy barrier and the forces needed for deploying and flat-folding are essential.

Different approaches can be employed to analyze nonlinear snapping, ranging from fine-scale to coarse-scale models: (1) finite element analysis (FEA), (2) bar-and-hinge models, (3) *quad soups*, and (4) *geometric incompatibility*. While FEA provides the most accurate representation of reality by quantifying strain energy and forces, it is computationally expensive and impractical for early design iterations. The bar-and-hinge method [Filipov et al. 2017; Liu and Paulino 2018] models material stretching via springs and bending through angular springs. This approach is relatively efficient and qualitatively captures structural behavior. However, in our case, when starting from a flat-folded configuration, the analysis is prone to bifurcation at singular states, making it unsuitable for our study. Both the quad soup and geometric incompatibility methods assume rigid panel motion. However, the quad soup method introduces gaps between all panels, while the geometric incompatibility approach specifies gaps between the two halves of the torus split along the extra foldlines. These gaps store the elastic energy, thereby creating an energy barrier. A comparison of the FEA, quad soup, and geometric incompatibility methods is presented in Appendix B.

Based on our comparison, we suggest the geometric incompatibility method (Section 4.1) for the earliest design phase. This method provides an initial estimate of the energy barrier and clarifies the factors that affect it. In particular, the width parameter of each toroid is determined to achieve desirable snapping properties. Subsequently, the quad soup approach (Section 4.2) is employed to run a more detailed simulation, enabling snapping force estimation and collision detection.

### 4.1 Incompatibility method

By observing physical prototypes, we experienced that most of the stress is concentrated along the extra foldlines during the snap. This observation motivated us to come up with the following incompatibility method. We assume that only the extra foldlines are realized by compliant hinges made of elastic material, e.g. rubber, with a spring-like behavior. As the faces are assumed to be rigid, all the deformation energy during the snap has to be accommodated by these elastic hinges. The extra foldlines separate the torus into two halves, each of which is a one-DOF mechanism. The basic idea of geometric incompatibility was already successfully used, e.g. in [Lee et al. 2023; Melancon et al. 2021; Zhou et al. 2023] to design and analyze origami-based multistable structures. The incompatibility measure used in [Melancon et al. 2021] is tailor-made for a special class of deployable structures with triangular faces, thus it cannot be applied to our toroids. A more general approach was used in [Lee et al. 2023; Zhou et al. 2023] where zero-length springs (with spring constant $k$) are introduced between corresponding endpoints of the elastic hinges to estimate the strain energy under the deformation. In [Lee et al. 2023], these springs were used to couple rigid-foldable

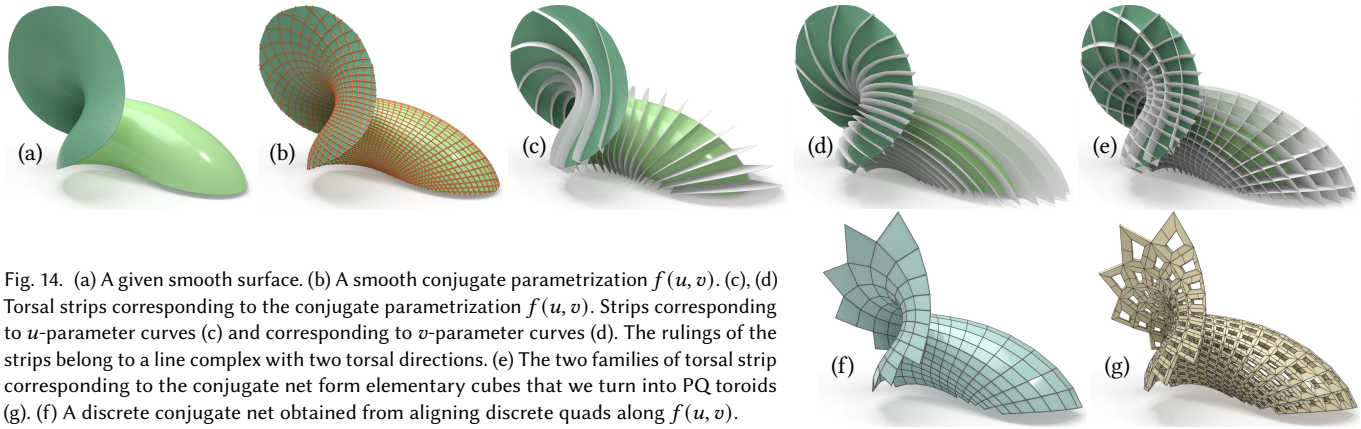


Fig. 14. (a) A given smooth surface. (b) A smooth conjugate parametrization $f(u, v)$. (c), (d) Torsal strips corresponding to the conjugate parametrization $f(u, v)$. Strips corresponding to $u$-parameter curves (c) and corresponding to $v$-parameter curves (d). The rulings of the strips belong to a line complex with two torsal directions. (e) The two families of torsal strip corresponding to the conjugate net form elementary cubes that we turn into PQ toroids (g). (f) A discrete conjugate net obtained from aligning discrete quads along $f(u, v)$.

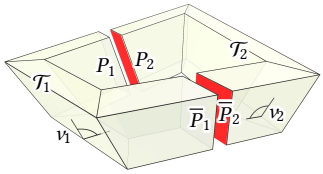


Fig. 15. The two half-toroids $\mathcal{T}_i$ ($i = 1, 2$): The shape of the cut parallelograms $P_i$ and $\overline{P}_i$ can be parametrized in dependence of the dihedral angle $\nu_i$.

structures to multistable ones, in contrast to the method of [Zhou et al. 2023], which assumes all hinges to be elastic. However, reducing the deformation to the vertices does not go along with the elastic hinge idea, as the springs have to be attached not only at the end points of the edges but also continuously between related point pairs. This elastic joint energy between the line-segments $[a, b]$ and $[a^\sigma, b^\sigma]$, where $\sigma$ denotes a rigid motion, can be computed as $E = \frac{1}{2}kD^2$ with

$$\begin{aligned} D^2 &:= \int_{x\in[a,b]} \|x - x^\sigma\|^2 \\ &= \tfrac{\|a-b\|}{3}\left(\|a - a^\sigma\|^2 + \|b - b^\sigma\|^2 + \langle a - a^\sigma, b - b^\sigma\rangle\right) \end{aligned} \tag{4}$$

according to [Nawratil 2017]. As $E$ is proportional to $D^2$ it is sufficient to consider this geometric quantity within the incompatibility approach.

*Remark* 4.1. Note that Eq. (4) can be seen as the zero-thickness limit case of the elastic energy used in [Botsch et al. 2006] for thin shells.

The computation of the incompatibility method can be subdivided into the following two steps:

*Step one.* We split the toroid along the extra foldlines, which form two parallelograms $P$ and $\overline{P}$, into two half-toroids $\mathcal{T}_1$ and $\mathcal{T}_2$ (see Fig. 15). Each one is now rigid-foldable with one degree of freedom. We take a dihedral angle $\nu_i$ along an uncut tube as a flexion parameter, which is denoted by $t_i$ after half-angle substitution; i.e. $t_i = \tan\frac{\nu_i}{2}$. Then, the shape of the two cut parallelograms $P_i$ and $\overline{P}_i$ can be computed in dependence of $t_i$ by solving a biquadratic equation [Stachel 2010], which can be done explicitly. This implies a parametrization of the rigid-folding for each half-toroid $\mathcal{T}_i$.

*Step two.* The basic idea is to compute for each configuration $\mathcal{T}_1(t_1)$ a rigid motion $\varsigma(t_1)$ and the configuration parameter $t_2(t_1)$ in such a way that the sum of squared distances (4) of corresponding edges of the parallelograms $P_1(t_1)$ and $P_2^\varsigma(t_2)$ as well as $\overline{P}_1(t_1)$ and $\overline{P}_2^\varsigma(t_2)$ is globally minimal (see Fig. 25-right). This registration problem with known correspondence can be solved using the approach of Horn [1987]. After translating the barycenter of the two parallelograms $P_i(t_i)$ and $\overline{P}_i(t_i)$ into the origin for $i = 1, 2$, we compute the best relative orientation of the half-toroids. This boils down to the computation of the largest eigenvalue of a $(4 \times 4)$-matrix. After discretizing the intervals of $t_1$ and $t_2$ we find the optimal value $t_2(t_1)$ by a brute force search.

## 4.2 Quad soup approach

In general, the incompatibility method cannot be used for the simulation of a folding motion on which an overall self-collision test can be based, due to the discontinuity of $\varsigma(t_1)$ and $t_2(t_1)$ demonstrated in Section B.1. As a consequence, this method will in general not provide reliable estimates of the forces needed for deploying and flat-folding. These problems can be resolved by the quad soup approach, where all hinges are elastic ones. The *nudged elastic band method* proposed in [Zhou et al. 2023] can be adopted for the elastic hinge energy (4). Moreover, the configuration implying the energy barrier of the incompatibility method can be used for the initial span of the elastic band[7]. Results of the quad soup approach are presented in Section B.2.

# 5 Design Pipeline and Results

We briefly explain how Sections 2, 3, and 4 come together in our design pipeline.

First, a given shape is approximated with a PQ-mesh and an offset direction is computed as described in Section 3. Here, the user has a design choice whether to go for a normal offset direction that will result in nearly equally thick toroids or to go for a general hyperbolic line congruence, as was done in Example 5.4.

Next, the PQ-toroids or T-toroids are generated. The height of each toroid can be chosen so that all toroids align, or it can be individually adjusted for each toroid. For choosing a good width and the correct placement of the extra foldlines, many criteria have to be taken into account. The energy barrier should not be too big (compare Appendix B) to prevent the structure from breaking.

[7] Linear interpolation between this configuration and the flat/deployable state.

Note that by decreasing the toroid width, the energy barrier can become arbitrarily small, see Remark B.1. At the same time, the toroid should not be too close to an infinitesimal flexibility; i.e. the stiffness should not be too low to obtain enough stability in the deployed state (compare Section 2.4). The same criteria must be taken into account when placing the extra foldlines.

For most toroids one can guarantee that one has no self-collision during the folding motion by adding the foldlines on the shorter edges of the toroid. For toroids with large width or height in comparison to the base quad this might not be possible and sliding can occur during the folding motion as explained in Section 2.2. This sliding motion can be detected using the quad soup approach by checking non-adjacent faces for intersection.

We suggest that the user first analyzes their choices with the incompatibility method, as it is the fastest approach. The quad soup technique can then give a more accurate picture including forces needed for deploying and flat-folding. When it comes to building real world modules, a finite element analysis that takes the material properties into account should be done eventually; compare Appendix B.3.2.

We proceed with some results of the design pipeline. All meshes were optimized for planarity of faces measured as distance of diagonals divided by circumference and coplanarity of normals measured as determinant of an edge and the corresponding normals. The results are given in Table 1.

Table 1. Planarity error (PE) of faces and coplanarity error (CE) of normals of the meshes used for the toroid generation.

| Fig. \ Error | PE Max | PE Min | PE Mean | CE Max | CE Min | CE Mean |
|---|---|---|---|---|---|---|
| 9 | 2e-7 | 3e-11 | 3e-8 | 8e-7 | 2e-13 | 2e-8 |
| 14 | 1e-7 | 8e-8 | 4e-5 | 1e-7 | 2e-11 | 2e-8 |
| 16 | 7e-6 | 1e-9 | 2e-6 | 3e-5 | 0 | 4e-6 |
| 17 | 3e-3 | 9e-8 | 4e-4 | 7e-2 | 2e-6 | 6e-3 |
| 18 | 4e-7 | 0 | 8e-8 | 9e-8 | 7e-12 | 2e-8 |
| 19 | 1e-7 | 7e-11 | 2e-8 | 1e-2 | 1e-12 | 5e-4 |
| 20 | 2e-4 | 5e-7 | 4e-5 | 4e-5 | 0 | 1e-4 |

*Example* 5.1. The base surface of the helicoid in Fig. 16 is a discrete conical Q-net. At each vertex star, there is a cone of revolution in tangential contact with the four adjacent faces. The cone axes form a discrete torsal congruence conjugate to the base surface. This congruence can be considered a discrete normal congruence. As a result of taking a discrete normal congruence for the torsal lines, the foldlines on the top faces at the corners of the quads are (almost) angle bisecting, and the height of all toroid modules is the same. While we mainly used opposite sides of the toroids to place the extra foldlines, in this example adjacent sides are used as well.

*Example* 5.2. In Fig. 14, we demonstrate how torsal strips can be found based on a conjugate parametrization of a given smooth surface. The torsal strips form a hyperbolic line congruence and thus can serve as a torsion free beam structure, compare [Pottmann et al. 2007b]. Such a beam structure could be filled with perfectly aligned PQ-toroids.

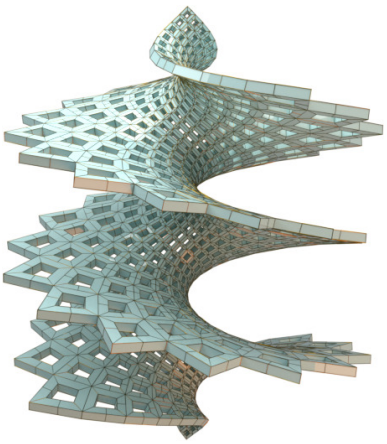

Fig. 16. Discrete helicoid. The base net is a discrete conical isothermic helicoid (cf. [Müller 2016]). The torsal lines are the discrete normals (the cone axes of the rotational cones in tangential contact with the four faces around each vertex). The heights of all toroid modules are the same (see Example 5.1).

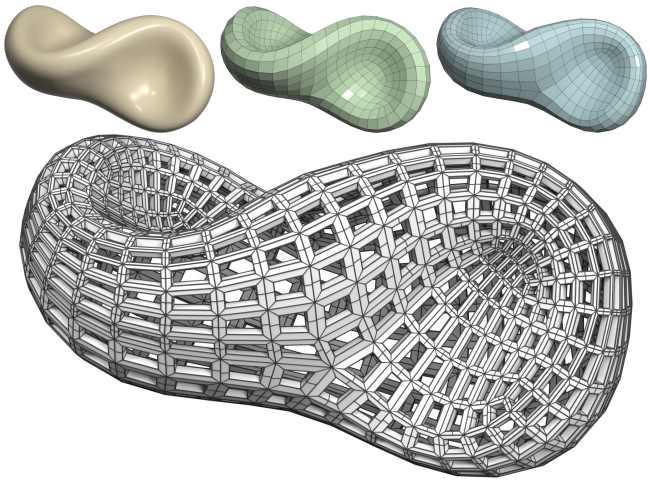

Fig. 17. Converting the diva_n reference surface (original design and 3D modeling by Ingrid Erb and Peter Ferschin) into a toroid structure. *Top left:* Reference surface as triangle mesh with ~70k faces. *Top center:* Quad mesh with 619 faces after re-meshing (see Sec. 3.3.1). Edges are roughly aligned with the principal directions and faces are almost planar. *Top right:* Q-net optimized for face-offset property. Computation time: 77.4 seconds. *Bottom:* Toroid structure with PQ-toroids. The base surface is the Q-net (*top right*).

*Example* 5.3. In Fig. 17, we started with the design of a couch inspired by the Moebius strip. The reference surface is provided as a dense triangle mesh. We derive a coarser PQ-net on it by quad re-meshing along the principal curvature lines. The resulting mesh is then further optimized to be a face-offset mesh. The final toroid structure consists of PQ-toroids.

*Example* 5.4. In a daytime-dependent shading system with toroids (see Fig. 18) the holes of the toroids can be aligned with the direction towards a particular position of the sun. This can be achieved by taking a Combescure transform of the base surface of the shading and place it "towards the sun" where (or better when) the sun should pass through the holes of the toroids. The lines connecting corresponding points of the base surface and the carefully placed Combescure transform generate the discrete line congruence needed

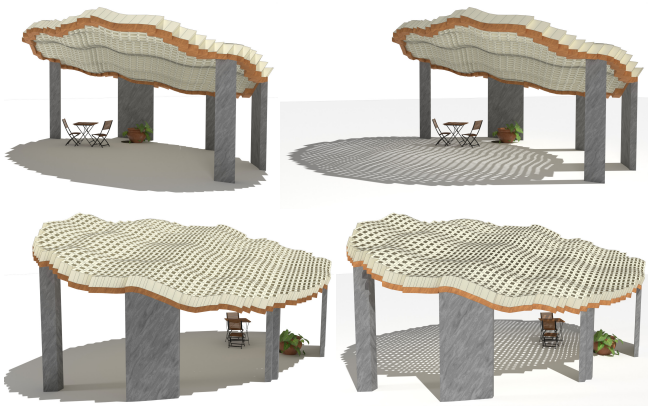

Fig. 18. Daytime-dependent shading system. The holes of the toroids can be aligned with the direction towards a particular position of the sun. *Left:* The strongest sunlight gets blocked, *right:* while later in the day some sunlight passes through the toroid structure.

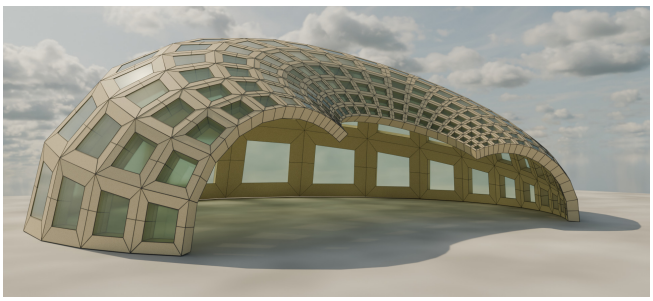

Fig. 19. A toroid structure over a so-called discrete isothermic net. In the rendering the holes are covered with a transparent or translucent material (e.g., some foil or some plexiglass).

for computing the toroids. In this way, the chosen sunlight direction (typically the strongest sunlight) gets blocked while later in the day some sunlight passes through the toroid structure. The height and thickness of the toroids can be used to let more and longer or less and shorter sunlight through the structure.

*Example* 5.5. In Fig. 19, we created a toroid structure based on a so-called discrete isothermic net. This is a Q-net where each face has a circumcircle and cross-ratio $-1$. This helps to obtain a mesh where all faces are close to squares.

*Example* 5.6. To put our computational approach to the test we fabricated a desktop model. The model is based on a Q-net with positive and negative curvature. The line congruence is a discrete normal congruence. This toroid structure consists of 60 PQ-toroids and is illustrated both as a rendering and as a photo of the built model in Fig. 20.

The compression achieved through flat folding is illustrated in Fig. 21. Close-up photos of individual modules in deployed and flat-folded states can be found in Fig. 2 and in video 1.mov in the supplemental materials.

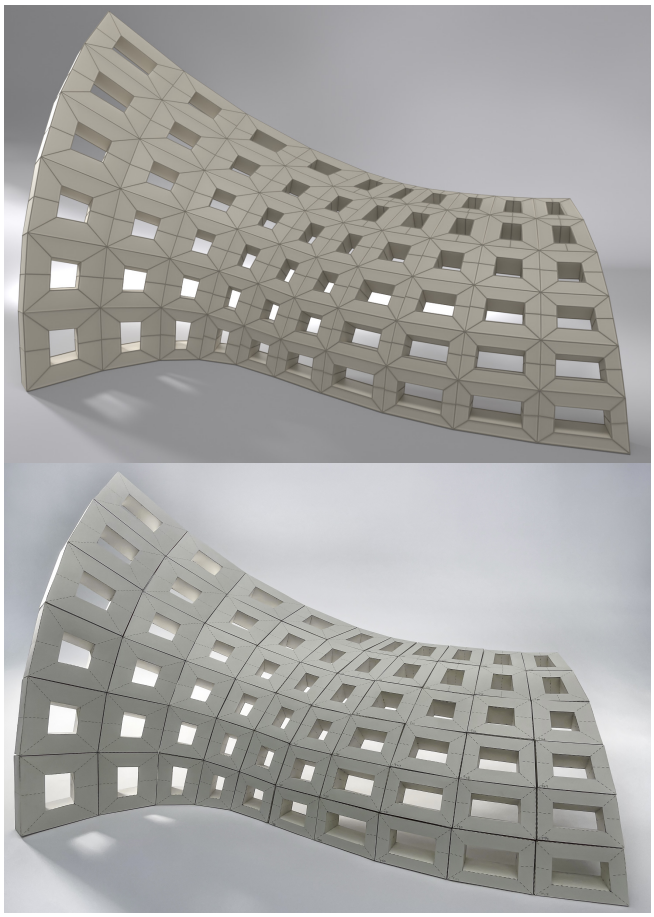

Fig. 20. *Top:* A rendered version of a toroid structure , and *bottom:* a photo of the same structure built from modeling cardstock. For convenience in production, each PQ-toroid is developed into four flat pieces: top, bottom, inner and outer rings with extra flaps to help the gluing process into volumetric toroidal shape. To assemble the structure, corresponding common faces in adjacent blocks are taped with double sided tape allowing to dismantle and re-assemble multiple times.

*Example* 5.7. We study a module (cf. Fig. 22) of the desktop model presented in Fig. 20 in more detail. For the 1-parametric set of extra foldlines we computed the energy barrier with respect to the incompatibility method (see Fig. 23-left). Moreover, according to Appendix A we evaluated for this family the stiffness of the deployed state (see Fig. 23-right). Note that the toroid used in the desktop model corresponds to the 50% value of the red foldline variation.

For an energy-efficient deployable design, which is infinitesimally very stable, the energy barrier should be low but the stiffness high. From this point of view it would be better to change the design of the toroid in the desktop model slightly to the one which corresponds approximately to 40% of the red foldline variation.

Finally, it should be mentioned that within numerical accuracy every foldline variation contains at least one design which gains an additional infinitesimal flexibility beside the infinitesimal translation of the inner ring to the outer one.

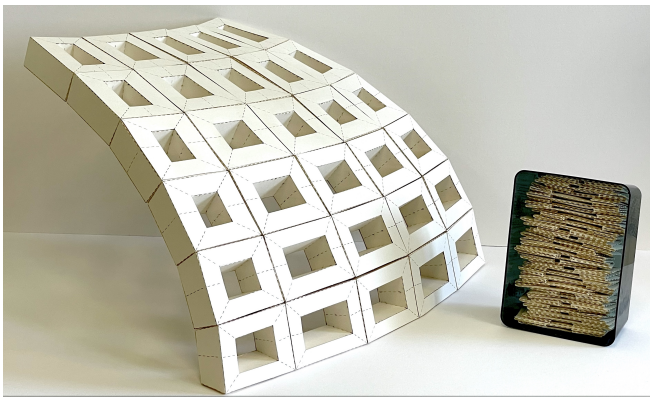

Fig. 21. The right half of the desktop model illustrated in Fig. 20 takes up $\sim 6982 cm^3$ space, while the same 30 PQ-toroids can be individually flat-folded and packed into a box of the size $\sim 1400 cm^3$ which is ~20% of the deployed volume. This percentage is ~15.7% for the entire structure with the total volume $\sim 19050 cm^3$ which can be fit into a box with $\sim 3000 cm^3$ volume, as the toroids of the other half are larger in average.

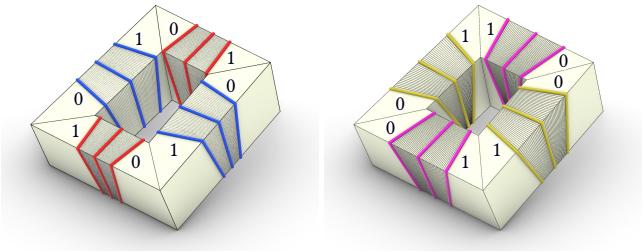


Fig. 22. Foldline variations within the interval $[0; 1]$: During the snap the inner ring moves upwards/downwards (Left/Right).

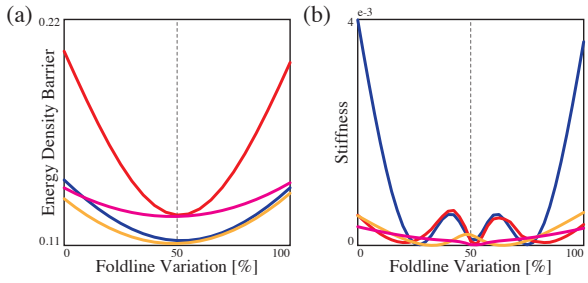


Fig. 23. The colors of the graphs of the energy density barrier (a) and stiffness (b) correspond to the fold variations illustrated in Fig. 22.

## 6 Discussions and Limitations

### 6.1 On the analyses

The *nudged elastic band (NEB) method* of the *quad soup approach* mentioned in Section 4.2 has its limitations as it over-detects self-collision. We noticed that some modules work, even if a collision is detected because the faces slide on each other. Therefore, a future implementation should restrict the infinitesimal relative motion of two non-adjacent quads which are in contact (i.e. their distance is below a certain threshold) to gliding motions [Pottmann and Ravani 2000].

Moreover, it would also be interesting to apply other geometric methods for evaluating the snappability of PQ-toroids which keep the integrity of the structure (i.e. it is not split up into two halves or separated quads) like the one presented in [Nawratil 2022] based on the intrinsic metric of the structure.

Note that this work does not contain any static analysis of the resulting PQ-toroidal gridshells, but their structural performance can also be improved by the underlying geometry of self-supporting quad surfaces [Vouga et al. 2012].

### 6.2 On the surface discretization

We established that the underlying meshes we need for the toroid assembly need to be discrete versions of conjugate nets. Although an infinite number of smooth conjugate nets exists on any surface, one cannot always hope to easily find a net that is well suited for discretization. If the conjugate directions get too close to the asymptotic directions of the surface, the quadrilaterals degenerate to lines. The best way to avoid asymptotic directions is to follow the principal curvature lines. However, the principal curvature lines will not align with the boundary curves of the surface in general.

Moreover, size control can be an issue when following principal directions. If the curvature variation is high, quadrilaterals might be too small or too large for practical use.

### 6.3 On fabrication-related considerations

When manufacturing actual modules, the panel thickness and hinge design must be carefully considered. Although thickness accommodation in rigid origami has been extensively explored [Chen et al. 2015; Lang et al. 2018; Tachi et al. 2011], directly applying these methods to the PQ-toroid poses challenges in realizing its flat-folded state. In this configuration, the additional creases intersect the other creases at right angles, which prevents existing methods from yielding valid solutions. However, since our approach already accounts for elastic bending and stretching of the materials, we can compensate for the thickness through minor controlled material deformations. Although thinner materials lead to reduced elastic deformation in the flat state, Appendix B demonstrates that thicker panels are necessary to achieve reliable snapping behavior, presenting an inherent trade-off in the design.

These trade-offs have a solution, at least for the desktop scale model in Fig. 20, which uses a $300 g/m^2$ craft cardboard sheet with a thickness of $0.3 mm$. This is approximately 0.5% of the average edge length, with the foldlines generated by folding along the dashed cut lines. The model exhibits both compact flat-folding and reliable snapping behavior. Given that the snapping mechanism is scalable, maintaining the same thickness-to-length ratio should allow this technique to be successfully applied to meter-scale models. Elastic materials, such as polypropylene sandwich panels featuring half-cuts for mountain creases and single or double V-cut hinges for valley creases on one side, are promising candidates for constructing the structure at a larger scale. Deployment can be actuated manually for the meter-scale models, but for enhanced reliability

and automation of the deployment process, pneumatic inflation could be adopted, as demonstrated in [Melancon et al. 2021].

### 6.4 Future research

Multistable toroids can be generalized in several different ways, which can then potentially tessellate other types of parametrizations. One direction is to start the construction from non-planar quads; i.e. skew quads (SQ) and generate SQ-toroids. Also, hexagonal meshes can be considered, since our study suggests that a similar approach can be taken to generalize a hexagonal T-toroid.

Another direction is to limit the variety of toroidal blocks and reconfigurable modular systems or other assemblies such as topologically interlocking blocks used in generalized versions of Abeille's structures [Anastas et al. 2024; Brocato and Mondardini 2012].

### 6.5 Conclusion

The goal of this paper was to design freeform shapes from multistable snapping origami-modules that possess a deployed state and a flat-folded state. Initial attempts were made with T-toroids (see [Lee et al. 2024]) only. However, understanding the design space of T-toroids in terms of discrete differential geometry shows that these structures were limited to convex Laguerre isothermic surfaces, see Section 3.2.1.

In contrast, the PQ-toroids that we introduced in this paper allow for a significantly larger design space. A PQ-toroid can always be aligned with a given planar quadrilateral and edgewise coplanar offset directions, as described in Section 2. A quadrilateral mesh with planar faces and edgewise coplanar normal vectors in the vertices is a discrete version of a conjugate mesh and a corresponding conjugate line congruence, as explained in 3.1. Note that any smooth surface admits such a parametrization and line congruence. Hence, theoretically, any surface can be approximated by a PQ-toroid structure.

Our energetic analysis of the bending behavior of the PQ toroids showed that they indeed exhibit a snapping behavior. Moreover, the analysis methods we presented can be used to choose the free design parameter in the surface assembly.

We built a desktop-sized model (see Fig. 20) as a proof of concept.

## Acknowledgments

The authors gratefully acknowledge the support by the Austrian Science Fund (FWF) through grants F77 (SFB "Advanced Computational Design"), DOI 10.55776/I4868 and DOI 10.55776/PAT1144724, as well as by the Japan Science and Technology Agency through grant JST ASPIRE JPMJAP2401 and the Japan Society for the Promotion of Science through grant JSPS 24KJ0648. We would also like to thank Florian Rist and Sobhan Samareh Rad for their support in the fabrication of our models. Furthermore, the authors would like to thank the anonymous reviewers for their valuable comments.

## References

Abdulrahman Almessabi, Xuwen Li, Amin Jamalimehr, and Damiano Pasini. 2024. Reprogramming multi-stable snapping and energy dissipation in origami metamaterials through panel confinement. *Philosophical Transactions A* 382, 2283 (2024), 20240005. https://doi.org/10.1098/rsta.2024.0005

Yousef Anastas, Olivier Baverel, and Maurizio Brocato. 2024. Design-to-construction workflow for free-form Abeille stone structures. In *Proceedings of IASS Annual Symposia*, Vol. 2024. International Association for Shell and Spatial Structures (IASS), 1–17.

Kensuke Ando, Bunji Izumi, Mizuki Shigematsu, Hiroki Tamai, Jun Matsuo, Yuki Mizuta, Takeshi Miyata, Jiro Sadanobu, Kai Suto, and Tomohiro Tachi. 2020. Lightweight rigidly foldable canopy using composite materials. *SN Applied Sciences* 2 (2020), 1–15.

Simon Bechert, Daniel Sonntag, Lotte Aldinger, and Jan Knippers. 2021. Integrative structural design and engineering methods for segmented timber shells-BUGA Wood Pavilion. In *Structures*, Vol. 34. Elsevier, 4814–4833.

Katia Bertoldi, Vincenzo Vitelli, Johan Christensen, and Martin Van Hecke. 2017. Flexible mechanical metamaterials. *Nature Reviews Materials* 2, 11 (2017), 1–11.

Alexander I. Bobenko and Yuri B. Suris. 2008. *Discrete differential geometry. Integrable structure*. Graduate Studies in Mathematics, Vol. 98. American Mathematical Society, Providence, RI. xxiv+404 pages.

David Bommes, Henrik Zimmer, and Leif Kobbelt. 2009. Mixed-integer quadrangulation. *ACM Trans. Graph.* 28, 3, Article 77 (July 2009), 10 pages.

Mario Botsch, Mark Pauly, Markus Gross, and Leif Kobbelt. 2006. PriMo: Coupled Prisms for Intuitive Surface Modeling. In *Symposium on Geometry Processing*, Alla Sheffer and Konrad Polthier (Eds.). The Eurographics Association.

Maurizio Brocato and Lucia Mondardini. 2012. A new type of stone dome based on Abeille's bond. *International Journal of Solids and Structures* 49, 13 (2012), 1786–1801.

Tian Chen, Julian Panetta, Max Schnaubelt, and Mark Pauly. 2021. Bistable auxetic surface structures. *ACM Transactions on Graphics (TOG)* 40, 4 (2021), 1–9.

Yan Chen, Rui Peng, and Zhong You. 2015. Origami of thick panels. *Science* 349, 6246 (2015), 396–400.

Robert Connelly, Idzhad Sabitov, and Anke Walz. 1997. The bellows conjecture. *Beiträge zur Algebra und Geometrie* 38, 1 (1997), 1–10.

Giulia Curletto and Luigi Gambarotta. 2016. Design of a composed origami-inspired deployable shelter: modeling and technological issues.. In *Proceedings of IASS Annual Symposia*, Vol. 2016. International Association for Shell and Spatial Structures (IASS), 1–10.

Adam Doliwa and Paolo M. Santini. 1997. Multidimensional quadrilateral lattices are integrable. *Physics Letters A* 233, 4 (1997), 365 – 372.

Michael Eigensatz, Martin Kilian, Alexander Schiftner, Niloy J Mitra, Helmut Pottmann, and Mark Pauly. 2010. Paneling architectural freeform surfaces. In *ACM SIGGRAPH 2010 papers*. 1–10.

Hongbin Fang, Suyi Li, Huimin Ji, and Kon-Wel Wang. 2017. Dynamics of a bistable Miura-origami structure. *Physical Review E* 95, 5 (2017), 052211.

Evgueni T. Filipov, Ke Liu, Tomohiro Tachi, Mark Schenk, and Gláucio H. Paulino. 2017. Bar and hinge models for scalable analysis of origami. *International Journal of Solids and Structures* 124 (2017), 26–45.

Evgueni T. Filipov and Maria Redoutey. 2018. Mechanical characteristics of the bistable origami hypar. *Extreme Mechanics Letters* 25 (2018), 16–26.

Evgueni T Filipov, Tomohiro Tachi, and Glaucio H Paulino. 2015. Origami tubes assembled into stiff, yet reconfigurable structures and metamaterials. *Proceedings of the National Academy of Sciences* 112, 40 (2015), 12321–12326.

Riccardo Foschi, Thomas C Hull, and Jason S Ku. 2022. Explicit kinematic equations for degree-4 rigid origami vertices, Euclidean and non-Euclidean. *Physical Review E* 106, 5 (2022), 055001.

Simon David Guest. 1994. *Deployable structures: concepts and analysis*. Ph. D. Dissertation. University of Cambridge PhD dissertation.

Chuck Hoberman. 1990. Expandable geodesic dome. *US Patent 4,942,700* (1990).

Berthold K. P. Horn. 1987. Closed-form solution of absolute orientation using unit quaternions. *J. Opt. Soc. Am. A* 4, 4 (Apr 1987), 629–642.

Alec Jacobson, Daniele Panozzo, et al. 2018. libigl: A simple C++ geometry processing library. https://libigl.github.io/.

Cai Jianguo, Deng Xiaowei, Zhou Ya, Feng Jian, and Tu Yongming. 2015. Bistable behavior of the cylindrical origami structure with Kresling pattern. *Journal of Mechanical Design* 137, 6 (2015), 061406.

Miura Koryo. 1985. Method of packaging and deployment of large membranes in space. *The Institute of Space and Astronautical Science report* 618 (1985), 1–9.

Anandaroop Lahiri and Phanisri Pradeep Pratapa. 2024. Improving mass lumping and stiffness parameters of bar and hinge model for accurate modal dynamics of origami structures. *Philosophical Transactions A* 382, 2283 (2024), 20240012.

Ernest P. Lane. 1942. *A Treatise on Projective Differential Geometry*. University of Chicago Press, Chicago, IL. ix+466 pages.

Robert J Lang, Kyler A Tolman, Erica B Crampton, Spencer P Magleby, and Larry L Howell. 2018. A review of thickness-accommodation techniques in origami-inspired engineering. *Applied Mechanics Reviews* 70, 1 (2018), 010805.

Munkyun Lee, Yuki Miyajima, and Tomohiro Tachi. 2023. Designing and Analyzing Multistable Mechanisms Using Quadrilateral Boundary Rigid Origami. *Journal of Mechanisms and Robotics* 16, 1 (03 2023), 011008.

Munkyun Lee, Kiumars Sharifmoghaddam, and Tomohiro Tachi. 2024. Multistable Polyhedral Origami Modules for Curved Surface Assembly. *Proceedings of International Association for Shell and Spatial Structures (IASS) Annual Symposia* (2024).

Munkyun Lee and Tomohiro Tachi. 2024. Design and Evaluation of Compliant Hinges For Deployable Thick Origami Structures. *Journal of the International Association for Shell and Spatial Structures* 65, 4 (2024), 238–247.
Julian Lienhard, Holger Alpermann, Christoph Gengnagel, and Jan Knippers. 2013. Active bending, a review on structures where bending is used as a self-formation process. *International Journal of Space Structures* 28, 3-4 (2013), 187–196.
Julian Lienhard and Christoph Gengnagel. 2018. Recent developments in bending-active structures. In *Proceedings of IASS annual symposia*, Vol. 2018. International Association for Shell and Spatial Structures (IASS), 1–8.
Ke Liu and Glaucio H Paulino. 2017. Nonlinear mechanics of non-rigid origami: an efficient computational approach. *Proceedings of the Royal Society A: Mathematical, Physical and Engineering Sciences* 473, 2206 (2017), 20170348.
Ke Liu and Gláucio H. Paulino. 2018. Highly efficient nonlinear structural analysis of origami assemblages using the MERLIN2 software.
Ke Liu, Tomohiro Tachi, and Glaucio H Paulino. 2019. Invariant and smooth limit of discrete geometry folded from bistable origami leading to multistable metasurfaces. *Nature communications* 10, 1 (2019), 4238.
Ke Liu, Tomohiro Tachi, and Glaucio H Paulino. 2021. Bio-inspired origami metamaterials with metastable phases through mechanical phase transitions. *Journal of Applied Mechanics* 88, 9 (2021), 091002.
Yang Liu, Helmut Pottmann, Johannes Wallner, Yong-Liang Yang, and Wenping Wang. 2006. Geometric modeling with conical meshes and developable surfaces. *ACM Trans. Graph.* 25, 3 (July 2006), 681–689.
Donald W. Marquardt. 1963. An Algorithm for Least-Squares Estimation of Nonlinear Parameters. *J. Soc. Indust. Appl. Math.* 11, 2 (1963), 431–441.
David Melancon, Benjamin Gorissen, Carlos J. García-Mora, Chuck Hoberman, and Katia Bertoldi. 2021. Multistable inflatable origami structures at the metre scale. *Nature* 592 (2021), 545–550.
Christian Müller. 2016. Planar discrete isothermic nets of conical type. *Beitr. Algebra Geom* 57, 2 (2016), 459–482.
Georg Nawratil. 2017. Point-models for the set of oriented line-elements – a survey. *Mechanism and Machine Theory* 111 (2017), 118–134.
Georg Nawratil. 2022. Snappability and singularity-distance of pin-jointed body-bar frameworks. *Mechanism and Machine Theory* 167 (2022), 104510.
Julian Panetta, Mina Konaković-Luković, Florin Isvoranu, Etienne Bouleau, and Mark Pauly. 2019. X-shells: A new class of deployable beam structures. *ACM Trans. Graph.* 38, 4 (2019), 1–15.
Sergio Pellegrino. 2001. Deployable structures in engineering. In *Deployable structures*. Springer, 1–35.
Stefan Pillwein and Przemyslaw Musialski. 2021. Generalized deployable elastic geodesic grids. *ACM Trans. Graph.* 40, 6 (2021), 1–15.
Helmut Pottmann, Michael Eigensatz, Amir Vaxman, and Johannes Wallner. 2015. Architectural geometry. *Computers & graphics* 47 (2015), 145–164.
Helmut Pottmann, Philipp Grohs, and Bernhard Blaschitz. 2010. Edge offset meshes in Laguerre geometry. *Adv. Comput. Math.* 33, 1 (2010), 45–73.
Helmut Pottmann, Yang Liu, Johannes Wallner, Alexander Bobenko, and Wenping Wang. 2007a. Geometry of multi-layer freeform structures for architecture. In *ACM SIGGRAPH 2007 Papers* (San Diego, California). Association for Computing Machinery, New York, NY, USA, 65–es.
Helmut Pottmann, Yang Liu, Johannes Wallner, Alexander Bobenko, and Wenping Wang. 2007b. Geometry of multi-layer freeform structures for architecture. In *ACM SIGGRAPH 2007 Papers* (San Diego, California) *(SIGGRAPH '07)*. Association for Computing Machinery, New York, NY, USA, 65–es.
Helmut Pottmann and Bahram Ravani. 2000. Singularities of motions constrained by contacting surfaces. *Mechanism and Machine Theory* 35, 7 (2000), 963–984. https://doi.org/10.1016/S0094-114X(99)00050-6
Helmut Pottmann and Johannes Wallner. 2001. *Computational line geometry*. Springer-Verlag, Berlin. x+563 pages.
Yingying Ren, Uday Kusupati, Julian Panetta, Florin Isvoranu, Davide Pellis, Tian Chen, and Mark Pauly. 2022. Umbrella meshes: elastic mechanisms for freeform shape deployment. *ACM Trans. Graph.* 41, 4 (2022), 152–1.
Szymon Rusinkiewicz. 2004. Estimating curvatures and their derivatives on triangle meshes. In *Proceedings. 2nd International Symposium on 3D Data Processing, Visualization and Transmission, 2004. 3DPVT 2004.* 486–493.
Robert Sauer. 1970. *Differenzengeometrie*. Springer-Verlag, Berlin-New York. 234 pages.
Bernd Schulze and Walter Whiteley. 2017. *Rigidity and scene analysis*. Chapman and Hall/CRC Press, USA, 1593–1632.
Kiumars Sharifmoghaddam, Rupert Maleczek, and Georg Nawratil. 2023. Generalizing rigid-foldable tubular structures of T-hedral type. *Mechanics Research Communications* 132 (2023), 104151.
Kiumars Sharifmoghaddam, Georg Nawratil, Arvin Rasoulzadeh, and Jonas Tervooren. 2020. Using flexible trapezoidal quad-surfaces for transformable design. In *Proceedings of IASS annual symposia*, Vol. 2020. International Association for Shell and Spatial Structures (IASS), 1–13.
Hellmuth Stachel. 2010. A kinematic approach to Kokotsakis meshes. *Computer Aided Geometric Design* 27, 6 (2010), 428–437.
Hellmuth Stachel. 2011. What lies between the flexibility and rigidity of structures. *Serbian Architectural Journal* 3, 2 (2011), 102–115.
Tomohiro Tachi. 2009a. Generalization of rigid-foldable quadrilateral-mesh origami. *Journal of the International Association for Shell and Spatial Structures* 50, 3 (2009), 173–179.
Tomohiro Tachi. 2009b. Simulation of rigid origami. *Origami* 4, 08 (2009), 175–187.
Tomohiro Tachi et al. 2011. Rigid-foldable thick origami. *Origami* 5, 5 (2011), 253–264.
Tomohiro Tachi and Koryo Miura. 2012. Rigid-foldable cylinders and cells. *Journal of the international association for shell and spatial structures* 53, 4 (2012), 217–226.
Chengcheng Tang, Xiang Sun, Alexandra Gomes, Johannes Wallner, and Helmut Pottmann. 2014. Form-finding with polyhedral meshes made simple. *ACM Trans. Graph.* 33, 4, Article 70 (July 2014), 9 pages.
Huu-Tai Thai, Tuan Ngo, and Brian Uy. 2020. A review on modular construction for high-rise buildings. In *Structures*, Vol. 28. Elsevier, 1265–1290.
Ashley P Thrall and CP Quaglia. 2014. Accordion shelters: A historical review of origami-like deployable shelters developed by the US military. *Engineering structures* 59 (2014), 686–692.
Michele Vidulis, Klara Mundilova, Quentin Becker, Florin Isvoranu, and Mark Pauly. 2025. C-Tubes: Design and Optimization of Tubular Structures Composed of Developable Strips. *ACM Trans. Graph.* 44, 4 (2025), 1–19.
Etienne Vouga, Mathias Höbinger, Johannes Wallner, and Helmut Pottmann. 2012. Design of Self-Supporting surfaces. *ACM Trans. Graphics* 31 (2012). http://www.geometrie.tugraz.at/wallner/selfsupporting.pdf Proc. SIGGRAPH.
Scott Waitukaitis, Peter Dieleman, and Martin van Hecke. 2020. Non-euclidean origami. *Physical Review E* 102, 3 (2020), 031001.
Chunlong Wang, Hongwei Guo, Rongqiang Liu, Zongquan Deng, Yan Chen, and Zhong You. 2024. Reconfigurable origami-inspired multistable metamorphous structures. *Science Advances* 10, 22 (2024), eadk8662.
Yuchen Wei and Sergio Pellegrino. 2017. Modular foldable surfaces: A novel approach based on spatial mechanisms and thin shells. In *4th AIAA Spacecraft Structures Conference*. 1345.
Hiromi Yasuda and Jinkyu Yang. 2015. Reentrant origami-based metamaterials with negative Poisson's ratio and bistability. *Physical review letters* 114, 18 (2015), 185502.
Hao Zhou, Matthew Grasinger, Philip Buskohl, and Kaushik Bhattacharya. 2023. Low energy fold paths in multistable origami structures. *International Journal of Solids and Structures* 265-266 (2023), 112125.
Yi Zhu and Evgueni T Filipov. 2024. Large-scale modular and uniformly thick origami-inspired adaptable and load-carrying structures. *Nature Communications* 15, 1 (2024), 2353.

## A Closeness to an Additional Infinitesimal Flexibility

The lengths $L_{i,j}$ of the edges $e_{i,j}$ with endpoints $x_i$ and $x_j$ do not change infinitesimally if there exist velocity vectors $v_i$ and $v_j$ such that $\Delta L_{i,j} = 0$ holds (see e.g. [Stachel 2011]) with

$$\Delta L_{i,j} := \langle x_i - x_j, v_i - v_j \rangle, \tag{5}$$

where the velocity vectors are not allowed to originate from a rigid-body motion of the complete structure. These so-called trivial flexes can be avoided by pinning down one link of the 6R loop to the fixed base $\Sigma_0$. Without loss of generality, we can assume that the system containing the axes $O_1$ and $O_6$ is fixed to $\Sigma_0$. As the inner ring can only make an infinitesimal translation in $z$-direction, due to the parallelogram-based cross-section of the tubes, we can also assume that the link between $I_1$ and $I_6$ is pinned to the base $\Sigma_0$. Note that this assumption only blocks the already known infinitesimal flex.

Therefore we could indicate the closeness to an additional infinitesimal flex by minimizing $\sum \Delta L_{i,j}^2$ under the normalizing condition

$$\sum \|v_i\|^2 = 1. \tag{6}$$

We prefer to optimize

$$\sum \frac{\Delta L_{i,j}^2}{L_{i,j}} \to \min \tag{7}$$

as then the result is proportional to the instantaneous change of the Cauchy strain energy of the structure interpreted as bar and hinge model. This is due to the fact, that the elastic strain energy stored

in a deformed bar $e_{i,j}$ equals

$$\frac{EA}{2}\frac{(L_{i,j}-L'_{i,j})^2}{L_{i,j}}, \tag{8}$$

where $A$ is the cross-sectional area of the bar, $E$ the Young modulus and $L'_{i,j}$ the length of the deformed bar. Summed up, the two infinitesimal flexes of the pinned inner and outer 6R-loops imply a stress in the toroid, as they do no fit in general. The extend the toroid resists unit-deformation (6) in response to this force is measured by (7). Hence, this closeness index can also be interpreted as stiffness.

Note that in our case only the eight horizontal edges, which do not belong to the fixed system $\Sigma_0$, can change their lengths as all other edges are R joints of the inner or outer loop, respectively. It remains to give the computation of the velocity vector $v_i$ of a vertex $x_i$ located on the axis $O_i$ of the outer ring. It is well known (see e.g. [Pottmann and Wallner 2001]) that this can be done by the formula

$$v_i = \overline{q}_i + q_i \times x_i \tag{9}$$

where $Q_i := (q_i, \overline{q}_i)$ is the instantaneous screw describing the infinitesimal motion of $O_i$ with respect to $\Sigma_0$ for $i = 2, \ldots, 5$. Assuming that the $O_i$s are given by their spear coordinates (see [Pottmann and Wallner 2001, Sec. 2.3]), the $Q_i$s can compactly be written as

$$Q_i := K_\omega \sum_{j=1}^{i-1} O_j \omega_j. \tag{10}$$

where $(\omega_1, \ldots, \omega_6)K_\omega$ denotes the ratio of angular velocities of the axes $O_1, \ldots, O_6$ of the outer loop with $K_\omega \in \mathbb{R} \setminus \{0\}$. Analogously, the velocity vectors on the inner ring are given by

$$Q_i := K_\iota \sum_{j=1}^{i-1} I_j \iota_j \tag{11}$$

where $(\iota_1, \ldots, \iota_6)K_\iota$ denotes the ratio of angular velocities of the axes $I_1, \ldots, I_6$ of the inner loop with $K_\iota \in \mathbb{R} \setminus \{0\}$.

It is important to note that the resulting velocity vectors only depend on $K_\iota$ for points of the inner ring and on $K_\omega$ for points on the outer ring. Therefore, (7) is a quadratic form in $K_\iota, K_\omega$ and (6) a quadratic side condition in these variables. This problem can be solved as a generalized eigenvalue problem. The resulting closeness index is demonstrated in Example 5.7.

## B Snapping Analysis: Comparative Example

For comparison of the different methods we use a T-toroid with a square $B$ of side length 1200 the and a square $T$ of side length 1661.88 as bottom and top face of the corresponding PQ-hexahedron. The planes of the outer and inner ring enclose $\pi/3$ with the bottom plane (see Fig. 28(b)). The height of the toroid is fixed with $H = 400$ but its width $W$ is varied from 100 to 500, as this geometric parameter can be selected separately for each module within a gridshell.

*Remark* B.1. Note that for the limit case of zero width the toroid degenerates into a closed 6R loop, which has the special property that all axes meet in a common point. Therefore, it can be seen as a spherical 6-bar mechanism, which has three degrees of freedom. As a consequence, the transition from the deployed to the flat-folded state can be done by a rigid-folding; i.e. the energy barrier is zero.

For the FEA, we have an additional free parameter because a thickness has to be assigned to the panels. In order to make the results comparable, we consider the energy density $E/V$; i.e. energy divided by the volume $V$, which remains constant during the deformation due to the chosen Poisson ratio of 0.5. Therefore, we also divided the results of the incompatibility method and quad soup approach by the area $A$ of the toroid, which is constant for these methods during the snap.

We have chosen a T-toroid for this comparative example as it has the nice property of possessing two folding modes, where the deployed state is a bifurcation configuration between them. In the first folding mode, the inner ring moves down from the base plane, and in the second mode up (see Fig. 28(c) and supplemental video 2.mov). In the remainder of this section, we call the latter one *high-energy mode* and the other one *low-energy mode*, due to the following results of our analysis.

We investigate the snapping behavior of the T-toroid by pulling apart along the measured *distance* in Fig. 28(b). We employ the following steps to enable direct comparison between the incompatibility method, quad soup, and the FEA, with different deployment control. First, we continuously measure the potential energy across states, spanning from flat configuration to full deployment in both low-energy and high-energy modes; here, the deployment control can be chosen for each method separately (not necessarily driven by the distance). Then, these measurements are illustrated as a deployment-energy plot, where the *deployment* $D$ is defined as the ratio of the distance illustrated in Fig. 28(b)-right to its maximum achievable value (i.e., 0% represents the flat state and 100% the fully deployed state). Here, the tangential slope of the deployment-energy plot corresponds to the required force. Computation of the incompatibility method took 1.9 seconds on an 8th generation Core i5 processor, the quad soup approach took 35.9 seconds on a 12th generation Core i7 processor. The finite element analysis took typically 20 to 30 minutes or more than an hour, if crumbling occurred, on a Core i9-9980XE processor.

### B.1 Results of the incompatibility method

For the computation of this example, we discretized the intervals of $t_1$ and $t_2$ into 120 steps.

Let us start by discussing the low-energy mode. In Fig. 24-left, the graphs of $D^2/A$ in dependence of $2 \arctan t_1$ for the five different widths are displayed. In Fig. 26 we have just converted the horizontal axis from the input angle into the deployment distance between the outer ring of the two half-toroids (explained in Fig. 28(b)-right) in order to facilitate the comparison with the FEA results. Moreover, this allows us to interpret the slopes of the latter graphs as force density, which are also visualized in Fig. 26. The ratio of the forces needed for flat-folding and deploying is given in Table 2.

Let us proceed with the discussion of the high-energy mode. Clearly, in this case the graph of $D^2/A$ in dependence of $2 \arctan t_1$ is still continuous (see Fig. 24-right) but $\varsigma(t_1)$ and $t_2(t_1)$ show some discontinuity. Note that in the general case, these discontinuities are expected, and that the continuity of $\varsigma(t_1)$ and $t_2(t_1)$ in the low energy mode is exceptional. The discontinuities arise because the

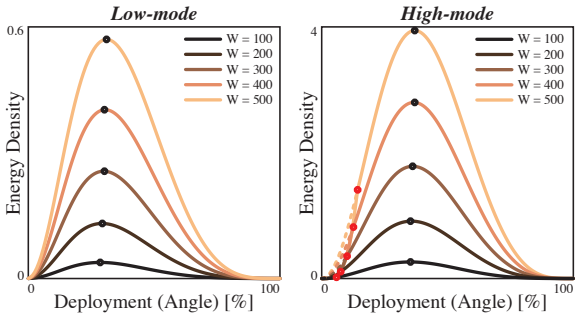


Fig. 24. The energy density computed by the incompatibility method with respect to the dihedral input angle. *Left:* Low energy mode. *Right:* High energy mode.

paths of the largest and second to largest eigenvalue of the $(4 \times 4)$-matrix mentioned in Section 4.1 are crossing each other (in the red highlighted singularity of the graphs in Fig. 24-right) during the snap. In order to get continuous energy-displacement plots and force-displacement plots (see Fig. 27), we follow the correct dashed paths in Fig. 24-right, even if the energy along them is a little higher towards the flat-folded state. The ratio of the forces needed for flat-folding and deploying is given in Table 3. Finally, the ratio of the energy barriers of the high mode and low mode is given in Table 4.

Table 2. Low energy mode: Absolute value of the ratio of the forces needed for flat-folding and deploying.

| Method \ Width | 100 | 200 | 300 | 400 | 500 |
|---|---|---|---|---|---|
| Incompatibility | 10.475 | 6.890 | 5.352 | 4.512 | 3.990 |
| Quad Soup | 11.354 | 7.302 | 5.537 | 4.609 | 4.069 |
| FEA | 2.173 | 2.879 | 5.893 | 7.823 | 7.202 |

Table 3. High energy mode: Absolute value of the ratio of the forces needed for flat-folding and deploying.

| Method \ Width | 100 | 200 | 300 | 400 | 500 |
|---|---|---|---|---|---|
| Incompatibility | 6.582 | 8.253 | 12.469 | 25.583 | 4011.611 |
| Quad Soup | 7.279 | 8.656 | 11.013 | 12.399 | 12.906 |
| FEA | 7.773 | 3.338 | 3.319 | 3.732 | 3.040 |

Table 4. Ratio of the energy barriers of the high mode and low mode.

| Method \ Width | 100 | 200 | 300 | 400 | 500 |
|---|---|---|---|---|---|
| Incompatibility | 6.865 | 6.946 | 6.973 | 6.955 | 6.914 |
| Quad Soup | 6.931 | 6.721 | 6.564 | 6.421 | 6.250 |
| FEA | 5.963 | 4.291 | 4.499 | 4.572 | 5.224 |

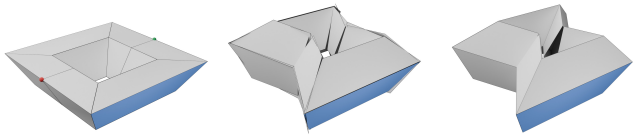

Fig. 25. Quad soup actuation. *Left:* Deployed state showing the fixed face (blue) and the constrained vertices (red, green). *Center:* Intermediate folding state at maximum energy of the quad soup. *Right:* Folding state of maximum energy resulting from the incompatibility method.

## B.2 Results of the quad soup approach

We adopt the computational setup presented in [Botsch et al. 2006; Zhou et al. 2023]. All faces of a toroid move independently subject to a rigid body motion while corresponding edges are connected via the elastic energy (4). We minimize this energy subject to the rigidity of faces while (i) keeping one face fixed and (ii) prescribing coordinates for a selected subset of toroid vertices. In the example shown in Fig. 25 the blue face remains fixed. The model is continuously actuated between the flat state and the deployed state by changing the x-coordinates of the red and green vertex (simulating a force pushing 'inwards').

The results meet the expectations that the incompatibility method has to overshoot the quad soup approach. This is due to the fact that in the quad soup approach the deformation energy during the snap is not concentrated along the extra foldlines but can distribute over the complete toroid; i.e. a large gap between the two half-toroids is split up into several smaller gaps between the 24 quads. Due to this refinement, the quad soup approach fits the results of the FEA better than the incompatibility method (please see Figs. 26 and 27 as well as Tables 2–4). Finally, it should be noted that the solution from the incompatibility method implies an upper bound for the energy of the quad soup approach, as it is also an admissible configuration for this approach.

## B.3 Finite element analysis

*B.3.1 FEA modeling.* We conducted FEA using Abaqus 2024 (Dassault Systèmes) to validate the snapping behavior and compare it with the incompatibility method. Fig. 28(a) shows the overall modeling strategy used to simulate the origami structure within the FEA interface.

Each panel of the representative block was modeled using shell elements, and S8R quadrilateral mesh elements were applied. To ensure proper connectivity, edges of equal length were divided into the same number of segments, allowing mesh nodes to align precisely between adjacent panels.

To simulate the folding behavior and accurately capture it in computation, we developed a new hinge modeling method. Based on the pin-joint array hinge proposed in [Lee and Tachi 2024], we implemented pin joints by connecting mesh nodes at identical locations using connector elements.

Each connector type was defined with 'Cartesian-type' for the translational degrees of freedom (x-, y-, and z-directions) and 'Rotation-type' for rotational degrees of freedom (Rx-, Ry-, and Rz-directions). While simple pin joints can be modeled using only the rotational

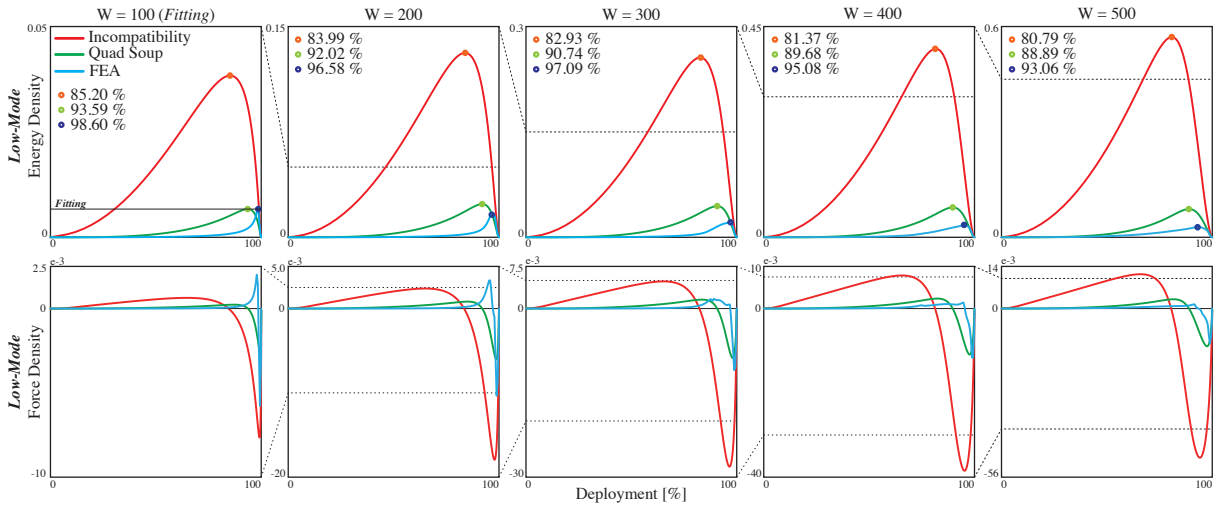


Fig. 26. Analysis comparison with incompatibility, soup, and finite element analysis of Low-mode. The upper row shows a deployment-energy density plot, and the lower row shows a gradient of energy density, which can be estimated as the force density. The energy barrier of the quad soup approach for $W = 100$ was scaled to match with the one of the FEA. This scaling factor is applied to all graphs of the quad soup approach and the incompatibility method.

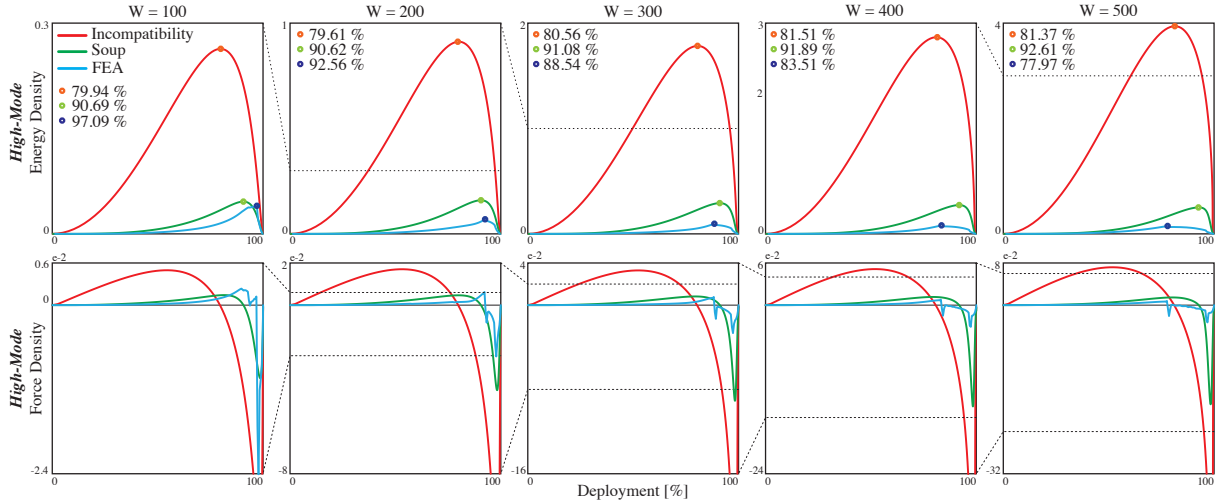


Fig. 27. Analysis comparison with incompatibility, soup, and finite element analysis of High-mode. Note that the graphs of the quad soup approach and the incompatibility method are scaled by the same factor used in Fig. 26.

setting, complex origami structures, especially at Degree-N-Vertices, often produce errors due to loops created in the master-slave relationships among multiple connected nodes. To avoid this, we also activated the translational degrees of freedom and assigned them high stiffness values to constrain them. By assigning equal stiffness to the x, y, and z translational directions, and likewise to the Rx, Ry, and Rz rotational directions, we ensured that each pin joint maintains the intended translational and rotational stiffness regardless of its position in the global coordinate system. This approach differs from other implementations [Almessabi et al. 2024; Lahiri and Pratapa 2024] which rely on local coordinate systems at each node connection, as our method achieves hinge behavior without generating local frames, simplifying the modeling process. To focus on the geometric behavior of the blocks, we did not set the complex physical behavior where actual creases occur, such as plastic or viscoelastic behavior. Instead, we used only linear stiffness values for each pin joint: translational stiffness of "$1.0 \times 10^6$ N/mm / edge nodes count" and rotational stiffness of "0.0001 N · mm/rad / edge nodes count".

Fig. 28(b) shows the boundary conditions applied to the model. Only one-quarter of the full block was modeled, and a mirror constraint was applied to the upper cut section along the YZ-plane (fixing x-translation, and Ry, Rz rotations), and translational constraints in the y-direction were applied at the additional crease lines to realize ideal hinge behavior without rotational stiffness. Note that although Fig. 28(b) illustrates the model in its deployed

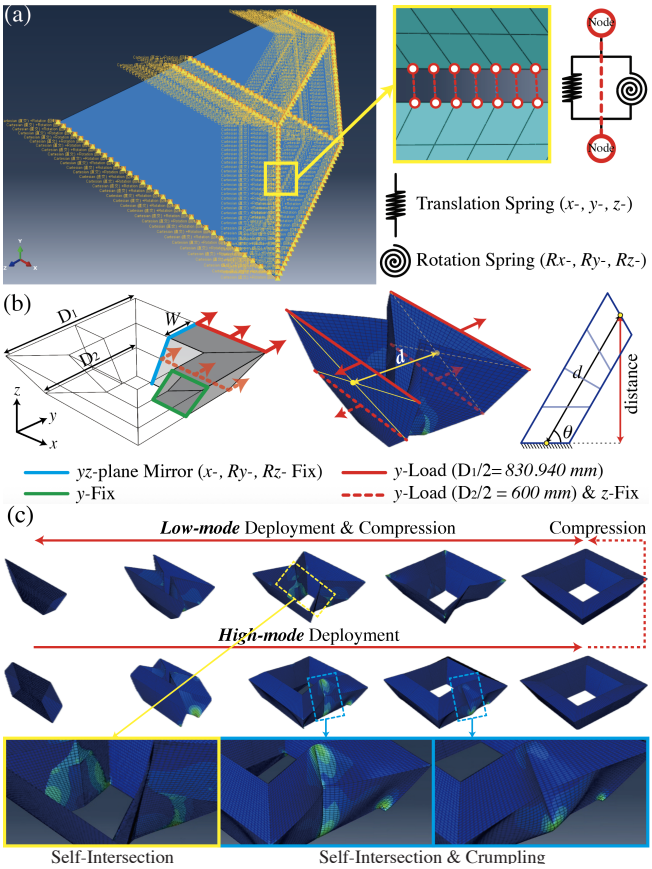


Fig. 28. (a) FEA modeling details, (b) Boundary conditions and deployment calculation, (c) Deployment and compression of motion of the low- and high-modes of $W$ = 400 case. The low-mode has self-intersection and the high-mode experiences severe panel deformation like crumpling.

state for clarity, the actual simulation was conducted from the flat configuration.

To simulate deployment, displacements of 830.94 mm and 600 mm were applied to the top and bottom edges of the topmost panel in the y-direction. Additionally, the bottom edge of this panel was constrained in the z-direction to prevent vertical translation. The model was analyzed using the dynamic implicit solver with the quasi-static setting.

The material properties used in the simulation are as follows. We adopted an approximate Elastic modulus of 1400 MPa and a density of $9.05 \times 10^{-10}$ t/mm$^3$, example of polypropylene. The Poisson ratio was set to 0.4999..., modeling the material as nearly incompressible with non-volumetric change to emphasize the geometric behavior and facilitate comparison with the incompatibility-based method. This is due to the fact that the complete energy goes into the deformation of the shape without any change in the internal energy of the material caused by the change of volume.

*B.3.2 FEA results.* Fig. 28(c) shows the low-mode and high-mode deployed configurations obtained through finite element analysis. In the low-mode configuration, self-intersections are observed around

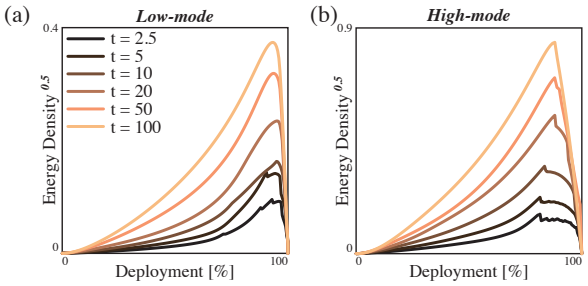


Fig. 29. The thickness parameter results of the (a) Low-mode, and (b) High-mode of the $W$ = 400 case, by finite element analysis. For plot clarification, we scaled the y-axis as the square root of energy density.

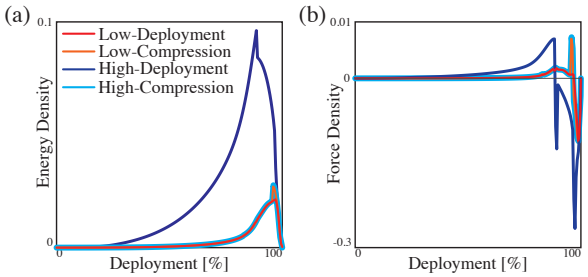


Fig. 30. Cycle loading results of the width 300 case. (a) Energy density, and (b) Force density plots.

the additional creases, while in the high-mode configuration, self-intersections occur near the edge tips, accompanied by severe crumpling of the panels around the added creases. This analysis was conducted to compare against geometry-based models such as the incompatibility and quad soup methods. Consequently, the simulation focused on capturing the elastic behavior of the panels without incorporating detailed physical conditions such as contact, plasticity, and damping. As the primary objective was to investigate the morphological characteristics and behavioral differences between deployments rather than to reproduce realistic structural responses, it should be noted that some self-intersections may appear in the results.

Given the pre-assembled curved surfaces using toroids, we only have two key design parameters that influence the energy barrier between stable states: the material thickness and the toroid width. Therefore, we carried out a parametric analysis based on these two parameters to examine their impact on structural behavior across different deployment modes.

Fig. 29 presents a comparison of the energy densities for the low-mode and high-mode configurations across varying panel thicknesses. For reference, both modes depicted in Fig. 28 (c) are based on a thickness of t = 10. As shown in Fig. 29 (b) $t$ = 2.5 - 50 cases, when an unexpected energy drop occurs, the energy curves deviate from the smooth, single-peak profile typically observed in geometry-based analyses above and instead display unstable behavior. In this study, we refer to such behavior as *crumpling*. Crumpling tends to occur more frequently at lower thicknesses and is observed in both the low and high modes. In particular, for the high mode, severe

local deformations are concentrated near the additional crease regions during deployment (see figure 28(c)), making it difficult to eliminate crumpling, even by increasing the thickness. Moreover, structures with lower thicknesses tend to exhibit unstable behavior after the peak, likely due to membrane-like movements and increased panel oscillations (see Fig. 29(b), $t = 10$ case). Overall, as the thickness increases, the total energy density tends to rise, and in cases without crumpling, the energy peak tends to appear earlier in the deployment process.

The blue curves in Figs. 26 and 27 show the finite element analysis results for the width ($W$) parameters. Overall, as the width increases, the energy density of the structure tends to rise, and the energy peak tends to occur earlier in the deployment process. Additionally, the energy curves exhibit a gentler slope at larger widths, indicating that panel deformation influences the structure from the early stages of deployment. For the low-mode configuration in Fig. 26, the energy curves increase relatively smoothly across all $W$ cases, forming a distinct single peak. In contrast, the high-mode configuration in Figs. 27 shows crumpling behavior at all width cases once deployment progresses. This crumpling occurs earlier as the structure becomes wider, suggesting that the panel deformation occurs from the early deployment stage, leading to earlier loss of structural stability. This behavior is also reflected in the force-density plots, where the post-crumpling regime shows unstable patterns. In wider structures, early-onset crumpling appears to hinder the structure from achieving a clear snap-through transition.

One notable observation is the resistance behavior of the toroid to compressive loading. In the fully deployed state, the additional crease lines become straightened, effectively forming axial members that enhance compressive resistance along the edge direction. Fig. 30 presents the energy and force density under cyclic loading for the case of $W = 300$. For the low-mode configuration, compression requires higher energy and force than deployment, with the load required for compression almost the same as the deployment load of the high-mode configuration. Furthermore, in the high-mode case, the structure turns into the low-mode configuration during compression (see Fig. 28(c)). This behavior occurs because the structure tends to follow the configuration with lower energy. Therefore, the high-mode toroid is characterized by difficult deployment but relatively easy compression, whereas the low-mode toroid exhibits easy deployment but relatively difficult compression.

## B.4 Conclusion of comparison

From the comparison between the incompatibility method and the FEA, we observed that the incompatibility method tends to overestimate the energy barrier. The quad soup approach has similar trends but performs better than the incompatibility.

The first notable trend is that the strain energy rises higher in the geometric incompatibility than in the FEA in the early deployment stage. Fig. 31 displays a double-log plot of deployment ($D$) versus energy. In the low-mode, the potential energy near the flat state (0%–10%) increases with deployment following a higher-order relationship ($D^{2.68}$–$D^{3.06}$) in the FEA model compared to a lower-order behavior ($D^{1.98}$–$D^{2.00}$) in the geometric incompatibility approach. This illustrates the slower potential energy response exhibited by

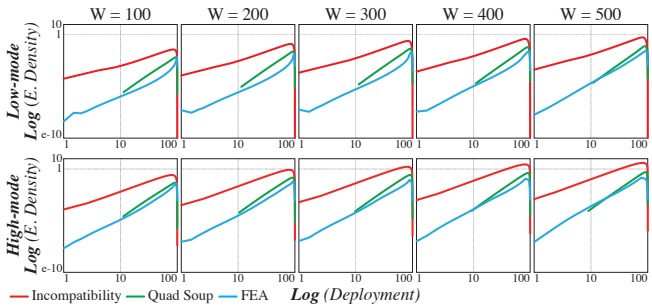


Fig. 31. Double-log plots of deployment-energy density. The upper row shows the Low-mode configurations, and the lower row shows the high-mode configuration.

the FEA model. The quad soup approach does not have the plots for these ranges because of the choice of actuation method; however, it has a similar or even higher order trend than the FEA for a latter range (10%–20%). We conjecture that this discrepancy arises because a thin shell initially accommodates the incompatibility through global bending of the panels, rather than panel stretching, having a delayed energy increase. Despite these limitations, the dependency of snapping behavior with respect to the geometric parameters of width is observed. This helps to identify the width dimension of the given toroid in the first design step.

Also, the degree of overestimation increases as the maximum incompatibility becomes more pronounced. In real materials or FEA models, the material tries to bend and buckle before it reaches the predicted high peak of energy from the stretching of the material. In its extreme case, crumpling occurs, for example in the high-energy mode, when the structure experiences a sharp drop in the strain energy before reaching the maximum (Figs. 27 and 29). The structure with thinner material and higher incompatibility is more prone to unpredictable crumpling, which is better avoided in the actual design. Empirically, we suggest choosing a thickness in the range 1.40%-13.98% of the characteristic length ($(D_1 + D_2)/2$) of the model to achieve a reliable snapping behavior; however, the behavior also depends on the width parameter.

For the desktop model the characteristic length ranges between ~61mm-193mm. With a 0.3mm thickness of the card stock used, the range is 0.15%-0.49% and yet, reasonable snapability is achieved without geometric thickness accommodation. The range of the width parameter was ~20mm-50mm which has been chosen as a relative value 60% of the maximum possible width of each individual toroid. The height parameter was a constant value 35mm for all the toroids.